



1 **Investigation of satellite vertical sensitivity on long-term retrieved lower tropospheric ozone trends**

2 Richard J. Pope<sup>1,2</sup>, Fiona M. O'Connor<sup>3,4</sup>, Mohit Dalvi<sup>3</sup>, Brian J. Kerridge<sup>5,6</sup>, Richard Siddans<sup>5,6</sup>, Barry G.  
3 Latter<sup>5,6</sup>, Brice Barret<sup>7</sup>, Eric Le Flochmoen<sup>7</sup>, Anne Boynard<sup>8,9</sup>, Martyn P. Chipperfield<sup>1,2</sup>, Wuhu Feng<sup>1,10</sup>,  
4 Matilda A. Pimlott<sup>1</sup>, Sandip S. Dhomse<sup>1,2</sup>, Christian Retscher<sup>11</sup>, Catherine Wespes<sup>12</sup> and Richard Rigby<sup>1,13</sup>

5 1: School of Earth and Environment, University of Leeds, Leeds, United Kingdom

6 2: National Centre for Earth Observation, University of Leeds, Leeds, United Kingdom

7 3: Met Office Hadley Centre, Exeter, United Kingdom

8 4: Department of Mathematics & Statistics, Global Systems Institute, University of Exeter, United Kingdom

9 5: Remote Sensing Group, STFC Rutherford Appleton Laboratory, Chilton, United Kingdom

10 6: National Centre for Earth Observation, STFC Rutherford Appleton Laboratory, Chilton, United Kingdom

11 7: Laboratoire d'Aérodologie/OMP, Université de Toulouse, Toulouse, France

12 8: LATMOS/IPSL, Sorbonne Université, UVSQ, CNRS, Paris, 75005, France

13 9: SPASCI, Ramonville-Saint-Agne, 31520, France

14 10: National Centre for Atmospheric Science, University of Leeds, Leeds, United Kingdom

15 11: European Space Agency, ESRIN, Frascati, Italy

16 12: Université libre de Bruxelles (ULB), Spectroscopy, Quantum Chemistry and Atmospheric Remote Sensing,  
17 Brussels, Belgium

18 13: Centre for Environmental Modelling and Computation, University of Leeds, Leeds, United Kingdom

19

20 Correspondence to: Richard J. Pope ([r.j.pope@leeds.ac.uk](mailto:r.j.pope@leeds.ac.uk))

21

22 **Key Points**

23

- 24 • Satellite lower tropospheric column ozone (LTCO<sub>3</sub>) trends in the northern hemisphere show small  
25 scale trends with large uncertainty ranges between 2008 and 2017.  
26 • Modelled LTCO<sub>3</sub> over that period is temporally stable and application of the satellite averaging  
27 kernels (AKs), accounting for the vertical sensitivity, to the model yields little impact on the  
28 simulated trends.

29

30 **Abstract:**

31 Ozone is a potent air pollutant in the lower troposphere and an important short-lived climate forcer (SLCF) in  
32 the upper troposphere. Studies investigating long-term trends in tropospheric column ozone (TCO<sub>3</sub>) have  
33 shown large-scale spatiotemporal inconsistencies. Here, we investigate the long-term trends in lower  
34 tropospheric column ozone (LTCO<sub>3</sub>, surface-450 hPa sub-column) by exploiting a synergy of satellite and  
35 ozonesonde datasets and an Earth System Model (UKESM) over North America, Europe and East Asia for the  
36 decade 2008-2017. Overall, we typically find small LTCO<sub>3</sub> linear trends with large uncertainty ranges from the  
37 Ozone Monitoring Instrument (OMI) and the Infrared Atmospheric Sounding Interferometer (IASI), while  
38 model simulations indicate a stable LTCO<sub>3</sub> tendency. Trends in the satellite a priori datasets show negligible



39 trends indicating year-to-year sampling is not an issue. The application of the satellite averaging kernels  
40 (AKs) to the UKESM ozone profiles, accounting for the satellite vertical sensitivity and allowing for like-for-  
41 like comparisons, has a limited impact on the modelled LTCO<sub>3</sub> tendency in most cases. While, in relative  
42 terms, this is more substantial (e.g. in the order of 100%), the absolute magnitudes of the model trends  
43 show negligible change. However, as the model has a near-zero tendency, artificial trends were imposed on  
44 the model time-series (i.e. LTCO<sub>3</sub> values rearranged from smallest to largest) to test the influence of the AKs  
45 but simulated LTCO<sub>3</sub> trends remained small. Therefore, the LTCO<sub>3</sub> tendency between 2008 and 2017 in  
46 northern hemispheric regions are likely small, with large uncertainties, and it is difficult to detect any small  
47 underlying linear trends due to inter-annual variability or other factors which require further investigation.

#### 48 **1. Introduction**

49 Tropospheric ozone (TO<sub>3</sub>) is a short-lived climate forcer (SLCF) and an important greenhouse gas (GHG;  
50 Myhre et al., 2013; Forster et al., 2021). TO<sub>3</sub> is also a hazardous air pollutant with adverse impacts on human  
51 health (Doherty et al., 2017; WHO, 2022) and agricultural/natural vegetation (Sitch et al., 2007; Hollaway et  
52 al., 2012). Since the pre-industrial (PI) period, anthropogenic activities have increased the atmospheric  
53 loading of ozone (O<sub>3</sub>) precursor gases, most notably methane (CH<sub>4</sub>) and nitrogen oxides (NO<sub>x</sub>) resulting in an  
54 increase in TO<sub>3</sub> of 25-50% since 1900 (Gauss et al., 2006; Lamarque et al., 2010; Young et al., 2013). The PI to  
55 present day (PD) radiative forcing (RF) from TO<sub>3</sub> is estimated by the Intergovernmental Panel on Climate  
56 Change (IPCC) to be 0.47 Wm<sup>-2</sup> (Forster et al., 2021) with an uncertainty range of 0.24-0.70 Wm<sup>-2</sup>.

57 During the satellite-era (i.e. since the mid-1990s), extensive records of TO<sub>3</sub> have been produced, e.g. by the  
58 European Space Agency Climate Change Initiative (ESA-CCI; ESA, 2019). However, the large presents of  
59 stratospheric O<sub>3</sub>, coupled with the different vertical sensitivities and sources of error associated with  
60 observations in different wavelength regions (e.g. Eskes and Boersma 2003; Ziemke et al., 2011; Miles et al.,  
61 2015) means large-scale inconsistencies in time and space exist between the records of satellite  
62 tropospheric column ozone (TCO<sub>3</sub>) (as shown by Gaudel et al., 2018).

63 The work by Gaudel et al. (2018) was part of the Tropospheric Ozone Assessment Report (TOAR), which  
64 represented a large global effort to understand spatio-temporal patterns and variability in TO<sub>3</sub>. However,  
65 their investigation of ozonesondes (2003-2012) and products from nadir viewing satellites in polar orbits  
66 (three from the Ozone Monitoring Instrument (OMI) (2005-2015/6) and two from the Infrared Atmospheric  
67 Sounding Interferometer (IASI) (2008-2016)) displayed discrepancies in the spatial distribution, magnitude,  
68 direction and significance of the TCO<sub>3</sub> trends. They noted that the records cover slightly different time  
69 periods but were unable to provide any definitive reasons for these discrepancies beyond briefly suggesting  
70 that differences in measurement techniques and retrieval methods were likely to be causing the observed  
71 spatial inconsistencies.

72 The vertical sensitivity of each retrieved product (function of measurement technique and retrieval  
73 methodology) used by Gaudel et al. (2018) will have had an impact on which part of the troposphere the O<sub>3</sub>  
74 signal is weighted towards. This was evident in the OMI and IASI TCO<sub>3</sub> trends, where OMI showed  
75 predominantly positive trends between 60°S and 60°N while the opposite was the case for IASI. The vertical  
76 sensitivity is represented by the “averaging kernel” (AK), which provides the relationship between  
77 perturbations at different levels in the retrieved and true profiles (Eskes and Boersma, 2003). Typically, for  
78 the products used by Gaudel et al., (2018), the peak AK sensitivities for TO<sub>3</sub> are in the 0-6 km range for OMI  
79 (Miles et al., 2015) and around 11-12 km for IASI (Keim et al., 2009). In the case of the Rutherford Appleton  
80 Laboratory (RAL) Space OMI data, used in Gaudel et al., (2018), TCO<sub>3</sub> values were derived from retrieved  
81 surface – 450hPa layer average mixing ratios applied also to the overlying 450hpa – tropopause layer using



82 ERA-Interim profiles. As the  $\text{TO}_3$  values were derived from different (UV and IR) sensors and methodologies  
83 whose vertical sensitivities differ, they were likely representing  $\text{O}_3$  controlled by different contributions of  
84 atmospheric processes (e.g. precursor emissions from the surface and stratosphere-troposphere exchanges).  
85 Therefore,  $\text{TCO}_3$  trends from the different satellite products are not necessarily expected to be similar.

86 In this study, we undertake the first assessment of spatio-temporal variability in satellite-derived lower  
87 tropospheric column ozone ( $\text{LTCO}_3$ , surface-450 hPa) from three instruments over a consistent decade  
88 (2008-2017). In combination with an Earth System Model (ESM), we aim to quantify the impact of year-to-  
89 year sampling, the satellite instrument uncertainties and the instrument vertical sensitivity on long-term  
90  $\text{LTCO}_3$  trends. We focus our analysis on North America, Europe and East Asia given their large emissions of  
91 ozone precursor gases and temporal variability. In our manuscript, **Section 2** discusses the  
92 satellite/ozonesonde datasets and model used, **Section 3** presents our results, and our discussion/  
93 conclusions are summarised in **Sections 4 and 5**.

## 94 **2. Methodology and Datasets**

### 95 **2.1. Satellite Datasets**

96 The satellite products (see **Table 1**) used here are from nadir-viewing polar-orbiting platforms providing  
97 ozone sub-column profiles. This includes ozone profile data from the OMI product developed by the RAL  
98 Space and the IASI products from the Laboratoire d'aérodynamique (IASI-SOFRID) and the Université Libre de  
99 Bruxelles, in collaboration with the Laboratoire Atmosphères, Observations Spatiales (ULB-LATMOS) (IASI-  
100 FORLI). OMI and IASI are on NASA's Aura and Eumetsat's MetOp-A satellites in sun-synchronous low Earth  
101 orbits with local overpass times of 13.30 and 9.30, respectively. OMI and IASI are ultraviolet-visible (UV-Vis)  
102 and infrared (IR) sounders with spectral ranges of 270-500 nm (Boersma et al., 2008, Boersma et al., 2011)  
103 and  $645\text{-}2760\text{ cm}^{-1}$  (Illingworth et al., 2011), respectively. OMI has a spatial footprint at nadir of  $24\text{ km} \times 13$   
104 km, while IASI measures simultaneously in four fields of view (FOV, each circular at nadir with a diameter of  
105 12 km) in a  $50\text{ km} \times 50\text{ km}$  square which are scanned across track to sample a 2200 km-wide swath (Clerbaux  
106 et al., 2009). The OMI retrieval scheme is based on an optimal estimation (OE) approach, produced by RAL  
107 Space, which is described in detail by Miles et al., (2015). The retrieval schemes for IASI-FORLI and IASI-  
108 SOFRID  $\text{O}_3$  are discussed in detail by Boynard et al., (2018) and Barret et al., (2020). In this work, the OMI  
109 data were filtered for good quality retrievals where the geometric cloud fraction was  $<0.2$ , the sub-column  
110  $\text{O}_3$  values were  $>0.0$ , the solar zenith angle  $<80.0^\circ$ , the retrieval convergence flag = 1.0 and the normalised  
111 cost function was  $<2.0$ . The IASI-FORLI data were filtered for a geometric cloud fraction  $<0.13$  (pre-filtered),  
112 degrees of freedom  $>2.0$ ,  $\text{O}_3$  values  $>0.0$ , solar zenith angle  $<80.0^\circ$  and the surface to 450 hPa sub-column  
113  $\text{O}_3$  / total column  $\text{O}_3 <0.085$ . The IASI-SOFRID data were provided on a  $1.0^\circ \times 1.0^\circ$  horizontal grid (i.e. level 3  
114 product, but at a daily temporal resolution – we use the daytime data in this study) with filtering already  
115 applied in Barret et al., (2020). Here, only  $\text{O}_3$  values  $>0.0$  were used. To remove systematic biases between  
116 the satellite records, ozonesondes were used to generate bias correction factors (2008-2017) to help  
117 harmonise the data sets. This is discussed in the Supplementary Material (i.e. **S1**). The application of the  
118 satellite AKs to the ozonesondes and the model is also discussed in **S1**. To investigate long-term trends over  
119 North America, Europe and East Asia, the Hemispheric Transport of Air Pollution (HTAP) regional sea-land  
120 mask (European Commission (2016); see **S2, Figure S2**), is used to generate average monthly time-series for  
121 each product over each region of interest. In Section 3.2, where we discuss the impact of satellite retrieval  
122 errors on derived  $\text{LTCO}_3$  linear trends, the OMI and IASI-FORLI retrieval errors are provided in their product  
123 files, but are not available for IASI-SOFRID. Therefore, while not a perfect metric to represent the error in the  
124 IASI-SOFRID data, we use the standard deviation in the monthly-spatial average of the regional time-series.



125 **2.2. United Kingdom Earth System Model (UKESM)**

126 The UK's Earth System Model, UKESM1.0, is a state-of-the-art ESM with fully interactive coupled component  
127 models (e.g. atmosphere, ocean, land surface, atmospheric chemistry), which has been developed by the UK  
128 Met Office and the Natural Environment Research Council (NERC). The detailed coupling of all the Earth  
129 System components is described by Sellar et al. (2019). However, in this study, we run UKESM1.0 in an  
130 atmosphere only configuration (e.g. similar to Archibald et al., (2020)). The aim is to use UKESM1.0 to  
131 investigate long-term trends in TO<sub>3</sub> and help explore inconsistencies between satellite records, so it is  
132 computationally more time efficient as only the atmospheric dynamics and chemistry components are  
133 simulated. Over the 2008-2017 time period (with a 1-year spin up), the UKESM1.0 model tracers and  
134 diagnostics (e.g. ozone, pressure) are output as 3D fields at sub-daily (6-hourly) time steps to allow robust  
135 comparisons between the model and satellite data sets (i.e. model-satellite spatio-temporal co-location to  
136 reduce representation biases and application of the satellite AKs to map the instrument vertical sensitivity  
137 onto the model yielding like-for-like comparisons).

138 Here, the UKESM1.0 land and atmosphere share a regular latitude–longitude grid with a resolution of 1.25°  
139 ×1.875° with 85 vertical levels on a terrain-following hybrid height coordinate with a model lid at 85 km  
140 above sea level (50 levels are below 18 km). All the key inputs to the model from other Earth system  
141 components (e.g. sea surface temperature (SST) and land surface vegetation) were prescribed from ancillary  
142 files. The ocean and ice forcing are represented by the monthly Reynolds sea ice and SSTs data from the  
143 National Oceanic and Atmospheric Administration (NOAA, [https://climatedataguide.ucar.edu/climate-](https://climatedataguide.ucar.edu/climate-data/)  
144 [data/](https://climatedataguide.ucar.edu/climate-data/)). Solar forcings are provided by Phase 6 of the Coupled Model Intercomparison Project (CMIP6;  
145 Matthes et al., 2017; Eyring et al., 2016), as is the stratospheric aerosol climatology to represent  
146 contributions from volcanic eruptions (Sellar et al., 2019). The land cover is provided from output from the  
147 land surface component of the ESM (JULES; Wiltshire et al., 2021) from a fully coupled historical simulation.  
148 Anthropogenic and biomass burning emissions from Hoesly et al. (2018) and van Marle et al. (2017) are  
149 prescribed for the period 2008 to 2014. After 2014, anthropogenic and biomass burning emissions are from  
150 the Shared Socioeconomic Pathway (SSP, Rao et al., 2017) 2-4.5 (i.e. a middle-of-the-road climate and  
151 emissions scenario).

152 Biological emissions are a climatology between 2001 and 2010 from the MEGAN-MACC data base  
153 (Sindelarova et al., 2014), while natural emissions are from the Precursors of Ozone and their Effects in the  
154 Troposphere (POET, [http://accent.aero.jussieu.fr/database\\_table\\_inventories.php](http://accent.aero.jussieu.fr/database_table_inventories.php)) based on 1990. Dry  
155 deposition of O<sub>3</sub> to the land surface is represented by the Wesley scheme, which is applied as in O'Connor et  
156 al., (2014). The model is also in a nudged or “specified dynamics” configuration (i.e. meteorological analyses  
157 are used to “nudge” the model's meteorological variables, i.e. u- and v-wind components, and potential  
158 temperature, towards reality; Telford et al., 2008) using 6-hourly reanalysis data from the European Centre  
159 for Medium-Range Weather Forecasts (ECMWF) ERA-Interim product. A similar configuration of UKESM1.0  
160 was used by Archibald et al., (2020), in which a thorough evaluation against multiple observations (e.g.  
161 surface, aircraft and satellite) was carried out.

162 **2.3. Trend Approach**

163 LTCO<sub>3</sub> trends are calculated using the linear least squares fit approach of van der A et al., (2006; 2008), and  
164 utilised by Pope et al., (2018) who investigated LTCO<sub>3</sub> trends. Here, the monthly LTCO<sub>3</sub> time-series are  
165 represented by the function:

166 
$$Y_t = C + BX_t + A\sin(\omega X_t + \phi) + N_t \quad (1)$$



167 where  $Y_t$  is the observed monthly  $\text{LTCO}_3$  for month  $t$ ,  $X_t$  is the number of months since the start of the record,  
 168  $C$  is the first month of the record,  $B$  is the monthly linear trend and  $A \sin(\omega X_t + \phi)$  is the seasonal model  
 169 component (Weatherhead et al., 1998).  $A$  is the amplitude,  $\omega$  is the frequency (set to 1 year;  $\omega = \pi/6$ ) and  $\phi$  is  
 170 the phase shift.  $C$ ,  $B$ ,  $A$  and  $\phi$  are the fit parameters from the linear least squares fit.  $N_t$  represents the model  
 171 errors/residuals. The linear trend uncertainty,  $\sigma_B$ , represents the trend precision and is calculated as:

$$172 \quad \sigma_B = \left[ \frac{\sigma_N}{n^2} \sqrt{\frac{(1+\alpha)}{(1-\alpha)}} \right] \quad (2)$$

173 where  $n$  is the number of years,  $\alpha$  is the autocorrelation in the residuals ( $N_t$ ) and  $\sigma_N$  is the standard deviation  
 174 in the residuals. As in van der A et al., (2006) and Pope et al., (2018), we calculate the autocorrelation for each  
 175 time-series using a lag of one-time step (i.e. one month). The autocorrelation in **Equation 1** is not accounted  
 176 for directly, so is factored into the trend uncertainty (**Equation 2**), as used and discussed by van der A et al.,  
 177 (2006) and Weatherhead et al., (1998), respectively.

### 178 **3. Results**

179 A detailed evaluation of UKESM1.0  $\text{LTCO}_3$  through comparisons with the three satellite products and  
 180 ozonesondes is presented in **S3**. Overall, UKESM1.0 robustly simulates  $\text{LTCO}_3$  spatially and seasonally in  
 181 comparison to the ozonesondes and satellite instruments (i.e. typically within the ozonesonde variability and  
 182 satellite uncertainty range).

#### 183 **3.1. UKESM1.0 and Satellite $\text{LTCO}_3$ Trends**

184  $\text{LTCO}_3$  trends from OMI, IASI-FORLI, IASI-SOFRID and ozonesondes are derived between 2008 and 2017 (i.e.  
 185 consistent time record for all instruments) using the linear-seasonal trend model (**Equation 1**). For each  
 186 satellite product, the corresponding UKESM1.0 time-series (with and without AKs) are analysed as well as  
 187 the satellite apriori. For the North America OMI metrics (**Figure 1 – top left, Table 2**), there is clear  
 188 seasonality in the apriori ranging between approximately 17.0 and 22.0 Dobson Units (DU). As this is based  
 189 on the climatology of McPeters et al., (2007), there is no trend and there is a very good model fit (i.e.  
 190  $R^2=1.0$ ). The key point is that, as a climatology, the apriori will have no trend but if there are substantial  
 191 temporal sampling differences between years, then an artificial trend could be introduced. OMI  $\text{LTCO}_3$   
 192 ranges between 20.0 and 27.0 DU with substantial variability. There is a drop in  $\text{LTCO}_3$  to 19.0 DU in 2009  
 193 before peaking at 25.0-27.0 DU between 2010 and 2015. Peak  $\text{LTCO}_3$  then drops to 22.0-24.0 DU in 2016 and  
 194 2017. As a result, the linear-seasonal trend model, which does not account for interannual variations such as  
 195 this, only has a fit skill of  $R^2=0.59$ . The corresponding OMI  $\text{LTCO}_3$  trend is -0.79 (-7.07, 5.48; 95% confidence  
 196 interval, p-value = 0.80) DU/decade showing a negligible trend with a large uncertainty range. Here, -0.79  
 197 DU/decade is the trend while the -7.07 and 5.48 DU/decade values are the 95% confidence interval. The  
 198 UKESM1.0  $\text{LTCO}_3$  time-series ranges between 17.0 and 22.0 DU with clear seasonality, though somewhat less  
 199 inter-annual variation than OMI, and the linear-seasonal trend model therefore has a considerably better fit  
 200 with  $R^2=0.95$ . The model trend has the opposite sign at 0.21 (-0.37, 0.78; p = 0.59) DU/decade. Here, the  
 201 model trend is near-zero with a relatively large uncertainty range (though not as sizable as OMI). When the  
 202 AKs are applied to the model, the trend switches sign to -0.57 (-1.58, 0.45, p = 0.98) DU/decade and the  
 203 linear-seasonal trend model fit decreases in skill to  $R^2=0.90$ . The trend switch of sign, though small, is  
 204 potentially linked to the application of the AKs, which also increases  $\text{LTCO}_3$  by 2.0-3.0 DU in general.

205 The IASI-FORLI  $\text{LTCO}_3$  time-series (**Figure 1 – top right**) tends to be lower than OMI and range between 17.0  
 206 and 22.0 DU. There is a substantial negative IASI-FORLI trend (-1.42 (-2.35, -0.50; p = 0.00) DU/decade);  
 207 **Table 2** though as suggested by Boynard et al., (2018) and Wespes et al., (2018), the input IASI Level-1 data



208 sets into the FORLI retrieval are not consistent with time; they suffer from a specific discontinuity in  
209 September 2010 which degrades the robustness of this trend. While we are aware of the artificial trend in  
210 the IASI-FORLI dataset, it is still a valuable long-term product allowing us to quantify multiple factors (e.g.  
211 impact of AKs on model tendencies/absolute values and year-to-year sampling stability – i.e. near-zero trend  
212 in the apriori). The apriori has a negligible trend but there is no clear seasonality in the apriori time-series. As  
213 a result, the linear-seasonal trend model has a more limited fit skill (i.e.  $R^2=0.67$ ). The impact of the satellite  
214 AKs appears to have less impact for IASI-FORLI as both UKESM1.0 and UKESM1.0+AKs have time-series  
215 ranging between approximately 17.0 and 21.0 (though slightly smaller UKESM1.0+AKs range) and linear-  
216 seasonal trend model fits of  $R^2=0.93$  and  $R^2=0.92$ , respectively. The corresponding trends are small at -0.13 (-  
217 0.75, 0.49;  $p = 0.67$ ) and -0.32 (-0.82, 0.20;  $p = 0.22$ ) DU/decade, but the introduction of the AKs does move  
218 the UKESM1.0 trend slightly towards that of the satellite. For IASI-SOFRID (**Figure 1 – bottom left**), there is  
219 little difference between any of the time-series as they all range between 16.0 and 21.0 DU with  
220 corresponding linear-seasonal trend model fits of  $R^2=0.94$  to 0.98 and negligible trends. The IASI-SOFRID and  
221 apriori trends are 0.12 (-0.59, 0.82;  $p = 0.74$ ) and 0.11 (-0.17, 0.39;  $p = 0.43$ ) DU/decade; **Table 2**,  
222 respectively, with the model showing near-zero trends in both cases. Given the close agreement between  
223 the satellite and apriori time series and fit metrics, it is suggestive that IASI-SOFRID  $TO_3$  is more closely  
224 confined to the apriori profile than are the other products. The ozonesondes show a substantial trend of -  
225 1.15 (-2.0, -0.10;  $p = 0.03$ ) DU/decade, while the model trend sampled as the sondes is -0.16 (-1.67, 1.35;  $p$   
226 =0.63) DU/decade. The co-located model and ozonesonde linear-seasonal trend model fits are  $R^2=0.62$  and  
227 0.64, respectively. The noise and lack of seasonality in the ozonesonde time-series is slightly unexpected  
228 given the reasonable density of stations over North America, though the spatial coverage and temporal  
229 sampling is much less than the satellite products.

230 In Europe, the OMI  $LTCO_3$  values are larger than in North America, ranging between 19.0 and 30.0 DU (**Figure**  
231 **2 – top left**). The same inter-annual variability exists, peaking between 2010 and 2015 with the minimum in  
232 2009. Hence, the linear-seasonal trend model, which does not represent interannual variation, does not  
233 have high skill and  $R^2=0.72$ . The corresponding trend is -0.80 (-7.29, 5.69;  $p = 0.80$ ) DU/decade, so has a  
234 similar direction and magnitude to that for North America, though is not substantial. The apriori ranges  
235 between 17.0 and 22.5 DU with a trend of -0.12 (-0.26, 0.03;  $p = 0.10$ ; **Table 2**) DU/decade. Given the  
236 relatively small trend and uncertainty range, unlike the OMI equivalent, it suggests there is unlikely to be an  
237 artificial trend arising through year-to-year changes in geographical sampling across the European region.  
238 UKESM1.0  $LTCO_3$  ranges between approximately 19.0 and 22.0 DU with a good linear-seasonal trend model  
239 fit of  $R^2=0.99$  and a trend of -0.11 (-0.50, 0.29;  $p = 0.59$ ) DU/decade. As for North America, when the OMI  
240 AKs are applied, the UKESM  $LTCO_3$  values systematically increase by 2.0-3.0 DU, move further away from the  
241 satellite apriori and more closely follow the variability of OMI (although  $R^2$  decreases slightly to 0.95). The  
242 trend tends towards that of OMI at -0.72 (-1.77, 0.32;  $p = 0.16$ ) DU/decade. As in the case of North America,  
243 the European IASI-FORLI apriori has no seasonal cycle (and moderate  $R^2$  of 0.48 in the linear-seasonal trend  
244 model fit) with a near-zero trend (0.09 (-0.09, 0.27;  $p = 0.32$ ) DU/decade) (**Figure 2 – top right, Table 2**). The  
245 IASI-FORLI data exhibit a substantial negative trend of -1.83 (-2.78, 0.89;  $p = 0.00$ ) DU/decade, again  
246 potentially attributable to step changes in the IASI Level-1 processor, with a good linear-seasonal trend  
247 model fit of  $R^2=0.92$ . UKESM1.0  $LTCO_3$  trends, without and with AKs applied, are -0.28 (-0.77, 0.20;  $p = 0.25$ )  
248 and -0.43 (-1.21, 0.35;  $p = 0.27$ ) DU/decade. Again, though a small change, the application of the AKs  
249 introduces a slight perturbation of the model trend compared to IASI-FORLI. The IASI-SOFRID apriori, ranging  
250 between 17.0 and 21.0 DU, has a trend of 0.17 (-0.12, 0.45;  $p = 0.24$ ) DU/decade with good fit skill of  $R^2=0.98$   
251 (**Figure 2 – bottom left**). The IASI-SOFRID and UKESM1.0 metrics, with and without averaging kernels





252 applied, are similar, with LTCO<sub>3</sub> trends of 0.05 (-0.91, 1.01; p = 0.92), -0.27 (-0.72, 0.19; p = 0.24) and 0.08 (-  
253 0.33, 0.49; p = 0.69) DU/decade, respectively, and with R<sup>2</sup> values between 0.93 and 0.98. The ozonesonde  
254 monthly regional means (**Figure 2 – bottom right**) has a more pronounced time-series than North America,  
255 yielding a less noisy time-series of LTCO<sub>3</sub>. Here, there is clear seasonality ranging between 17.0 and 24.0 DU  
256 with a large R<sup>2</sup> value of 0.95. The ozonesonde trend is relatively small at -0.61 (-1.39, 0.17; p = 0.12)  
257 DU/decade while the UKESM1.0 equivalent is more substantial at -0.96 (-1.56, 0.35; p = 0.00) DU/decade.

258 For East Asia, OMI LTCO<sub>3</sub> again has both a pronounced seasonal cycle and inter-annual variability (19.0-27.0  
259 DU), consistent with the other two regions discussed above (**Figure 3 – top left**). This yields a moderate skill  
260 fit to the linear-seasonal trend model of R<sup>2</sup>=0.52 and near-zero trend (-0.09 (-7.88, 7.70; p = 0.98)  
261 DU/decade). The apriori has a trend of -0.25 (-0.71, 0.22; p = 0.29) DU/decade, so year-to-year sampling  
262 changes could be influencing the robustness of OMI retrieved time-series in this region. However, both the  
263 instrument and apriori trend uncertainties intersect with 0.0. UKESM1.0 LTCO<sub>3</sub> ranges between  
264 approximately 16.0 and 22.0 DU with a good fit R<sup>2</sup> of 0.98. Like the other regions, the application of the OMI  
265 AKs increases the model values systematically by several DUs. The UKESM1.0 LTCO<sub>3</sub> trend is -0.16 (-0.94,  
266 0.62; p = 0.67) DU/decade, which is small, but the AKs increase the trend magnitude to -0.62 (-2.24, 1.00; p =  
267 0.44) DU/decade, which moves it away from the OMI trend. IASI-FORLI (**Figure 3 – top right, Table 2**), like  
268 the other two regions, has a substantial negative trend of -1.52 (-2.16, 0.88; p = 0.00) DU/decade. The apriori  
269 again exhibits virtually no seasonal cycle but non-zero year-to-year variation so a low fit skill of R<sup>2</sup>=0.21 and  
270 shows a near-zero trend of -0.03 (-0.22, 0.16; p = 0.76) DU/decade. For UKESM1.0, the East Asian seasonal  
271 range is much larger than other regions, ranging between 17.0 and 27.0 DU (i.e. seasonal amplitude of  
272 approximately ±5.0 DU). When the AKs are applied, this range shrinks to approximately 19.0 to 23.0 DU,  
273 more in-line with the IASI-FORLI LTCO<sub>3</sub> values. The corresponding model trends are -0.03 (-0.62, 0.56; p =  
274 0.93) DU/decade and -0.29 (-0.80, 0.22; p = 0.25) DU/decade, so the AKs are pushing the model tendency  
275 towards that of the instrument, though the impact is small in absolute terms (large in relative terms). IASI-  
276 SOFRID and its apriori LTCO<sub>3</sub> seasonality are again very similar, ranging between 16.0 and 21.0 DU with very  
277 little interannual variability and with linear seasonal trend model fit skills of R<sup>2</sup>=0.96 and 0.98 (**Figure 3 –**  
278 **bottom left, Table 2**). The IASI-SOFRID and apriori linear trends are therefore also consistent at -0.19 (-1.01,  
279 0.63; p = 0.65) and -0.15 (-0.73, 0.58; p = 0.82) DU/decade. The UKESM1.0 seasonal variability is again large,  
280 between 17.0 and 26.0 DU, and, as in the case of IASI-FORLI, when the instrument AKs are applied to the  
281 model, the seasonal range shrinks (i.e. 16.0-22.0 DU) to be much closer to those of the retrieval and its prior.  
282 The model trends are -0.42 (-0.97, 0.13; p = 0.12) and -0.24 (-0.67, 0.20; p = 0.28) (with AKs) DU/decade,  
283 where there is a minor shift in the model tendency towards that of IASI-SOFRID and its prior. For the  
284 ozonesondes (**Figure 3 – bottom right**), there is a substantial LTCO<sub>3</sub> trend of 3.17 (0.16, 6.17; p = 0.04)  
285 DU/decade with a fit skill of R<sup>2</sup>=0.79, which is larger than those for North America and Europe. LTCO<sub>3</sub>  
286 increases from 18.0-25.0 in 2008 to 21.0-28.0 in 2011. This remains similar in 2012 and 2013 before  
287 dropping by several DUs between 2014 and 2017. The UKESM1.0 sampled as the ozonesondes has  
288 considerably less inter-annual variability with a smaller trend of 0.37 (-0.90, 1.64; p = 0.56) DU/decade.  
289 Therefore, UKESM1.0 and the satellite product trends are generally smaller (in magnitude) than the  
290 ozonesonde tendencies. However, it is worth considering that there are only a few sites (e.g. Hong Kong and  
291 Taiwan) where ozonesonde data is available in East Asia.

### 292 3.2. Influence of Satellite Averaging Kernels on UKESM1.0 LTCO<sub>3</sub>

293 To investigate the impact of applying the satellite averaging kernels to UKESM1.0, and thus learn something  
294 about vertical sensitivity influence on retrieved LTCO<sub>3</sub>, three different metrics are considered for the 2008 to  
295 2017 time-period. These are the absolute LTCO<sub>3</sub> value, amplitude of the LTCO<sub>3</sub> seasonal cycle and the linear



296 trend. These metrics are compared for the satellite, the satellite  $\pm$  error term, the apriori, UKESM1.0 and  
297 UKESM1.0+AKs for the three regions discussed above.

298 From **Figure 4**, average OMI L<sub>TCO</sub><sub>3</sub> is approximately 22.0, 24.0 and 23.0 DU for North America, Europe and  
299 East Asia, respectively. This represents a substantial deviation away from the apriori values of 17.5, 20.0 and  
300 16.0 DU, respectively. However, the average error term for OMI L<sub>TCO</sub><sub>3</sub> is sizeable at approximately  $\pm 8.0$  to  
301  $\pm 9.0$  DU for all regions. The average UKESM1.0 value for each region is approximately 19.5, 21.5 and 19.0 DU  
302 but the application of the AKs increases this by several DU to 22.0, 24.0 and 21.0 DU. In comparison, mean  
303 values for both IASI products vary less between the three geographical areas: IASI-FORLI (IASI-SOFRID) L<sub>TCO</sub><sub>3</sub>  
304 values are 20.0 (18.5), 19.0 (18.5) and 22.0 (18.0) DU, respectively. The corresponding error ranges, in  
305 comparison with OMI, are smaller between 17.0 and 23.0 (16.0 and 21.5), 16.0 and 21.5 (16.0 and 21.0) and  
306 18.0 and 23.5 (14.5 and 21.5) DU for North America, Europe and East Asia, respectively. With the IASI-FORLI  
307 AKs applied to UKESM1.0, L<sub>TCO</sub><sub>3</sub> decreases from 19.5 to 19.25 DU, 21.25 to 19.5 DU and 22.75 to 21.25 DU  
308 for the three regions. For IASI-SOFRID, there is a decrease from 21.0 to 19.5 DU in Europe and a decrease  
309 from 22.0 to 19.5 DU in East Asia, while no change occurs in North America. Overall, OMI has the largest  
310 error range and the application of the AKs to UKESM1.0 systematically increases the model L<sub>TCO</sub><sub>3</sub> time-  
311 series by several DU. The opposite occurs for the IASI products where there is a smaller decrease to  
312 UKESM1.0 L<sub>TCO</sub><sub>3</sub> of 1.0-2.0 DU. The error ranges are also smaller than that of OMI.

313 In terms of the L<sub>TCO</sub><sub>3</sub> seasonal amplitude (**Figure 5**), OMI (including the error terms) is approximately 2.6  
314 (for all) DU, 3.3-3.8 DU and 2.3-2.6 DU for North America, Europe and East Asia. The apriori seasonal  
315 amplitude ranges from 2.7 to 2.9 DU across the regions. The IASI-FORLI averages (including the error terms)  
316 tend to be lower than OMI but have similar seasonal ranges. North America, Europe and East Asia have  
317 amplitudes of 2.3-2.5 DU, 2.3-2.5 DU and 1.6-1.8 DU, respectively. It is noteworthy that this seasonal cycle is  
318 despite the IASI-FORLI prior exhibiting virtually no seasonal cycle at all. IASI-SOFRID has a European range of  
319 2.4-2.6 DU, and comparable ranges for North America and East Asia at 1.8-2.5 DU and 2.3-3.0 DU. Therefore,  
320 seasonal amplitude in IASI-SOFRID is more sensitive to the error metric but as the “error” term is based on  
321 the L<sub>TCO</sub><sub>3</sub> standard deviation, given the lack of an error term in the product, it is unsurprising that there is  
322 more variability in the seasonal amplitude. For the OMI comparisons, the application of the AKs to  
323 UKESM1.0 shifts the simulated amplitude slightly upwards from 2.0 to 2.1 DU, 3.1 to 3.3 DU and 4.0 to 4.4  
324 DU for the respective regions. The IASI-FORLI AK impacts are a decrease from 1.9 to 1.4 DU, 3.0 to 2.1 DU  
325 and 4.2 to 1.9. For IASI-SOFRID, the corresponding impact on UKESM1.0 is 2.2 to 2.4 DU, 3.3 to 2.9 and 4.5 to  
326 3.2 DU. Therefore, the OMI AKs have a minimal impact, increasing the model seasonal amplitude by 0.1-0.3  
327 DU, but the IASI products suppress the simulated amplitude by 1.0-2.0 DU at the most extreme.

328 The impact of the satellite L<sub>TCO</sub><sub>3</sub> error terms on the derived linear trends are shown in **Figure 6**. For OMI,  
329 the range in trends calculated (i.e. satellite  $\pm$  error term) is approximately -1.50 (-7.04, 4.04;  $p = 0.59$ ) to -  
330 0.09 (-6.98, 6.81;  $p = 0.98$ ) DU/decade, -1.65 (-6.92, 3.62;  $p = 0.53$ ) to 0.05 (-7.44, 7.53;  $p = 0.99$ ) DU/decade  
331 and -1.05 (-6.61, 4.52;  $p = 0.70$ ) to 0.87 (-8.24, 9.98;  $p = 0.85$ ) DU/decade for North America, Europe and East  
332 Asian, respectively. The IASI-FORLI trends (i.e. satellite  $\pm$  error term) are substantial, ranging from -1.50 (-  
333 2.51, -0.50;  $p = 0.00$ ) to -1.34 (-2.21, -0.47;  $p = 0.00$ ) DU/decade, -1.87 (-2.87, -0.87;  $p = 0.00$ ) to -1.80 (-2.72, -  
334 0.88;  $p = 0.00$ ) DU/decade and -1.62 (-2.27, -0.98;  $p = 0.00$ ) to -1.42 (-2.06, -0.78;  $p = 0.00$ ) for the three  
335 regions, respectively. The corresponding IASI-SOFRID trends were 0.09 (-0.48, 0.66;  $p = 0.75$ ) to 0.14 (-0.59,  
336 0.88;  $p = 0.70$ ) DU/decade, -0.07 (-0.91, 0.78;  $p = 0.87$ ) to 0.16 (-0.74, 1.07;  $p = 0.72$ ) DU/decade and -0.30 (-  
337 1.02, 0.42;  $p = 0.41$ ) to -0.08 (-0.73, 0.58;  $p = 0.82$ ), respectively. Therefore, only the IASI-FORLI trends (i.e.  
338 satellite  $\pm$  error term) are substantially different from zero (i.e.  $p < 0.05$ ). However, that is likely due in part





339 to discontinuities in the Level-2 input meteorological data used to generate this version of the product  
340 (Boynard et al., 2018).

341 The application of the OMI AKs to UKESM1.0 had the largest impacts on the simulated trends with changes  
342 in a negative direction from of 0.21 (-0.37, 0.78;  $p = 0.59$ ) to -0.57 (-1.58, 0.45,  $p = 0.98$ ) DU/decade, -0.11 (-  
343 0.50, 0.29;  $p = 0.59$ ) to -0.72 (-1.77, 0.32;  $p = 0.16$ ) DU/decade and -0.16 (-0.94, 0.62;  $p = 0.67$ ) to -0.62 (-  
344 2.24, 1.00;  $p = 0.44$ ) DU/decade for the respective regions. IASI-FORLI AKs introduced small decreases from -  
345 0.13 (-0.75, 0.49;  $p = 0.67$ ) to -0.32 (-0.82, 0.20;  $p = 0.22$ ) DU/decade, -0.28 (-0.77, 0.20;  $p = 0.25$ ) to -0.43 (-  
346 1.21, 0.35;  $p = 0.27$ ) DU/decade and -0.03 (-0.62, 0.56;  $p = 0.93$ ) to -0.29 (-0.80, 0.22;  $p = 0.25$ ) DU/decade.  
347 IASI-SOFRID AKs introduced small increases in the LTCO<sub>3</sub> trend from -0.24 (-0.85, 0.37;  $p = 0.44$ ) to -0.04 (-  
348 0.53, 0.45;  $p = 0.87$ ) DU/decade, -0.27 (-0.72, 0.19;  $p = 0.24$ ) to 0.08 (-0.33, 0.49;  $p = 0.69$ ) DU/decade and -  
349 0.42 (-0.97, 0.13;  $p = 0.12$ ) to -0.24 (-0.67, 0.20;  $p = 0.28$ ) DU/decade.

350 As the absolute model trends are small, it is difficult to determine the impact of the AKs on the simulated  
351 trends. In relative terms, it can have impacts of several 100% but the model and model+AK trend ranges  
352 (95% confidence interval) always intersect. Therefore, in an attempt to derive more substantial UKESM1.0  
353 LTCO<sub>3</sub> trends (without and with AKs applied), to assess the maximum impact the AKs can have on UKESM  
354 LTCO<sub>3</sub> trends, the modelled data were sorted from lowest to highest and the trend re-calculated. In North  
355 America, this approach forced positive model trends, sub-sampled to OMI, IASI-FORLI and IASI-SOFRID, of  
356 0.73 (0.22, 1.25;  $p = 0.00$ ), 0.64 (-3.50, 4.77;  $p = 0.76$ ) and 0.80 (0.41, 1.19;  $p = 0.00$ ) DU/decade. When the  
357 AKs were applied, it yielded trends of -0.74 (-1.89, 0.40;  $p = 0.20$ ), 0.55 (0.08, 1.03;  $p = 0.02$ ) and 0.58 (0.24,  
358 0.92;  $p = 0.00$ ) DU/decade. In Europe, this forced positive trends model trends, of 0.62 (0.14, 1.10;  $p = 0.01$ ),  
359 0.37 (-0.05, 0.79;  $p = 0.08$ ) and 0.46 (0.09, 0.84;  $p = 0.01$ ) DU/decade, respectively. With the AKs applied, the  
360 trends become 0.47 (-0.51, 1.44;  $p = 0.34$ ), 0.28 (-0.38, 0.94;  $p = 0.40$ ) and 0.10 (-0.32, 0.51;  $p = 0.64$ )  
361 DU/decade. Finally, in East Asia, the forced model trends are 0.90 (0.34, 1.47;  $p = 0.00$ ), 0.66 (0.15, 1.17;  $p =$   
362 0.01) and 0.63 (0.26, 1.00;  $p = 0.00$ ) DU/decade. The application of the AKs introduced model trends of 1.02  
363 (-0.04, 2.09;  $p = 0.05$ ), 0.08 (-0.44, 0.61;  $p = 0.75$ ) and 0.20 (-0.20, 0.61;  $p = 0.31$ ) DU/decade.

364 Even with forced trends in the UKESM1.0 regional time-series, the trends are relatively small (i.e. typically  
365 less than 1.0 DU/decade in magnitude). Therefore, the application of the AKs to the forced UKESM LTCO<sub>3</sub>  
366 time-series still yields small scale change tendencies and there is overlap in the two model trend uncertainty  
367 ranges (i.e. 95% confidence level). However, in relative terms, the trend changes are larger (e.g. >100% in  
368 multiple cases) and there is often a shift of the modelled LTCO<sub>3</sub> trend uncertainty range either intersecting  
369 or no longer intersecting with zero (i.e. a shift in  $p$ -value regime from  $<0.05$  to  $>0.05$ ). Therefore, in modelled  
370 and satellite datasets with more substantial trends, the impacts of the AKs, and thus the satellite vertical  
371 sensitivity, on LTCO<sub>3</sub> trends would be much greater and potentially help pinpoint sources of differences  
372 between satellite products in their TO<sub>3</sub> temporal evolution.

#### 373 4. Discussion

374 Investigation of satellite LTCO<sub>3</sub> focussed on 2008 to 2017, representing a decade of overlap of the OMI and  
375 IASI records. The analysis focussed on North America, Europe and East Asia as these regions are subject to  
376 large emissions of and temporal changes in O<sub>3</sub> precursor gases. LTCO<sub>3</sub> is typically spatially homogeneous  
377 with shallow gradients between background and source-induced O<sub>3</sub> concentrations. Secondly, individual  
378 retrievals of LTCO<sub>3</sub> are subject to multiple issues (e.g. influences on radiative transfer and vertical sensitivity  
379 of stratospheric ozone, cloud and other particulates, surface spectral reflectivity/emissivity and temperature  
380 profile) which can result in noisy LTCO<sub>3</sub> time-series at high resolution (e.g. when gridded on a scale of 0.5° or  
381 1.0°). Both of these factors supported analysis at a regional scale (e.g. continental scale).



382 Ideally, this analysis would have utilised several more records (e.g. several UV-Vis and IR products) to  
383 quantify long-term trends in L<sub>TCO<sub>3</sub></sub> and investigate the potential reasons for any discrepancies, as shown by  
384 Gaudel et al., (2018) for T<sub>CO<sub>3</sub></sub>. While RAL Space, and other providers, have generated UV-Vis profile O<sub>3</sub>  
385 products for more instruments, e.g. from the Global Ozone Monitoring Experiment 1 & 2 (GOME-1 & GOME-  
386 2) and the SCanning Imaging Absorption spectroMeter for Atmospheric CartographY (SCIAMACHY), the  
387 GOME-1 and SCIAMACHY records do not overlap for as long with IASI and step changes in the GOME-2A  
388 Level-1 processing scheme used to produce the available L<sub>TCO<sub>3</sub></sub> Level-2 version mean it is not sufficiently  
389 homogeneous (see Pope et al., (2023)). For the IR instruments, other potential sensors include the  
390 Tropospheric Emissions Spectrometer (TES; Richards et al., 2008) and the RAL Space IASI Extended Infrared  
391 Microwave Sounding (IMS; Pimlott et al., 2022) scheme applied to IASI. Unfortunately, the TES record only  
392 covers 2005 to 2013, with decreasing spatial coverage with time, and at the time of this work the IASI-IMS  
393 product had only been processed on a sub-sampled basis of 1 in 10 days.

394 In this work, we some find discrepancies in the observed long-term tendencies from the utilised L<sub>TCO<sub>3</sub></sub>  
395 products in these northern hemispheric regions. The OMI product is subject to large-scale interannual  
396 variability over the 2008-17 decade, in comparison with which the underlying linear trends are small in  
397 absolute terms with large confidence ranges (i.e. 95% confidence intervals) intersecting with zero. .  
398 However, the OMI L<sub>TCO<sub>3</sub></sub> product has been shown to be stable over this period relative to ozonesondes by  
399 Pope at el., (2023). IASI-FORLI has substantial negative L<sub>TCO<sub>3</sub></sub> tendencies, but this is driven by a specific  
400 discontinuity in 2010 due to inhomogeneity in Eumetsat (water vapour, temperature) data used in IASI-  
401 FORLI Level-2 processing (Boynard et al., 2018; Wespes et al., 2018). It induces an artificial drift that explains  
402 the substantial negative L<sub>TCO<sub>3</sub></sub> trends reported here and in Gaudel et al., (2018). The IASI-SOFRID L<sub>TCO<sub>3</sub></sub> and  
403 apriori are very similar, with little inter-annual variability, which suggests that the IASI-SOFRID O<sub>3</sub> retrieval in  
404 this height-range is more constrained by the apriori (i.e. less T<sub>O<sub>3</sub></sub> sensitivity than the other products).  
405 Importantly, analysis of the three products' apriori L<sub>TCO<sub>3</sub></sub> records show negligible trends meaning that year-  
406 to-year sampling differences (i.e. the number of retrievals used in the spatial-monthly regional averages) are  
407 not skewing long-term satellite trends. In summary: any underlying linear trend in L<sub>TCO<sub>3</sub></sub> occurring during  
408 the decade 2008-17 was masked by interannual variability in the OMI retrieval and by constraint to the  
409 apriori in the IASI-SOFRID retrieval and, although substantial for IASI-FORLI retrieval, that is believed to be  
410 due to changing meteorological input to the data processing.

411 For UKESM1.0, the model exhibits negligible temporal variability in L<sub>TCO<sub>3</sub></sub> for all regions and instruments'  
412 samplings. Modelled L<sub>TCO<sub>3</sub></sub> trends never exceeded 1.0 DU/decade in magnitude, all of which were deemed  
413 to be insignificant due to large associated p-values by the linear-seasonal trend model detailed in **Section 2.4**  
414 and **Equations 4 & 5**. The ozonesondes for each region were included to ground truth the model and satellite  
415 trends. The North American sites' L<sub>TCO<sub>3</sub></sub> time-series was relatively noisy and exhibited considerable inter-  
416 annual variability in its seasonal cycle. The comparatively low level of inter-annual variability in the European  
417 UKESM1.0 record of L<sub>TCO<sub>3</sub></sub> was in good agreement with the ozonesondes, however, and so was its low  
418 trend, providing confidence in the model over that region. For East Asia, the interannual variability differed  
419 substantially between UKESM1.0 and ozonesondes and the reported ozonesonde trend was significantly  
420 much larger than for UKESM1.0. Therefore, when considering UKESM1.0 and the ozonesondes, no consistent  
421 L<sub>TCO<sub>3</sub></sub> trends can be determined for any of the regions. Overall, taking all data sets into account, L<sub>TO<sub>3</sub></sub>  
422 appears to have neither increased nor decreased markedly over these three regions between the beginning  
423 and end of the study decade (i.e. 2008 to 2017).

424 One key aspect of this work was to exploit UKESM1.0 to determine the importance of vertical sensitivity on  
425 retrieved L<sub>TO<sub>3</sub></sub> and how this influences the reported long-term tendency. In terms of the absolute model



426 trends (with and without the satellite AKs), the impact on L<sub>TCO</sub><sub>3</sub> was small with typically near-zero  
427 tendencies and large uncertainty ranges (i.e. the 95% confidence interval). In relative terms, the changes in  
428 model trend values were more substantial in the order of 100%. To explore this further, the UKESM1.0 L<sub>TCO</sub><sub>3</sub>  
429 time-series (with and without the satellite AKs) were sorted from lowest to highest (based on annual  
430 averages) to impose the most substantial trend in the model data. When the trends were re-calculated, the  
431 largest model L<sub>TCO</sub><sub>3</sub> trends ranged between 0.37 and 0.90 DU/decade. When the AKs were applied, the  
432 L<sub>TCO</sub><sub>3</sub> trends ranged from -0.74 to 1.02 DU/decade. Again, in relative terms, this represents a relatively large  
433 impact of the AKs on simulated L<sub>TO</sub><sub>3</sub> tendencies but in absolute terms, these are small changes. Though, it  
434 should be noted that many of the 95% confidence intervals for these trends either shifted to intersect with  
435 zero or vice versa once the AKs were applied to the model. Gaudel et al., (2018) suggested two potential  
436 reasons for the T<sub>CO</sub><sub>3</sub> trend discrepancies in their study:

- 437 - Time varying instrument biases/drift.
- 438 - The impact of satellite vertical sensitivity.

439 A further two important reasons are:

- 440 - Changes over time in latitude/longitude domains sampled by satellite sensors (e.g. GOME-1 has  
441 substantial issues after 2003).
- 442 - The time-period used for the trend analysis.

443 According to Boynard et al., (2018) and Wespes et al., (2018), the IASI-FORLI-v20151001 products has an  
444 artificial negative drift with time explained by a discontinuity found in the Level-2 meteorological inputs  
445 taken from Eumetsat. However, in the near future, a new consistent IASI-FORLI ozone climate data record  
446 will be available using homogeneous Level-1 and Level-2 Eumetsat meteorological data. Analysis of OMI  
447 L<sub>TCO</sub><sub>3</sub> by Pope et al., 2023 showed OMI L<sub>TCO</sub><sub>3</sub> to be temporally stable against ozonesondes. A similar  
448 analysis (not shown here) indicates IASI-SOFRID L<sub>TCO</sub><sub>3</sub> to also be temporally stable with near-zero drift in  
449 bias. For the satellite vertical sensitivity, some of our results were unexpected. While the application of the  
450 AKs to UKESM1.0 can substantially shift the simulated absolute L<sub>TO</sub><sub>3</sub> values and squash/stretch the seasonal  
451 amplitude, the impact on the simulation L<sub>TCO</sub><sub>3</sub> tendencies are small in absolute terms. In relative terms, the  
452 impacts can be large (e.g. 100% change in trend rate). However, as the UKESM1.0 simulated L<sub>TCO</sub><sub>3</sub> trends  
453 are generally near-zero, it is difficult to confidently say either way if the vertical sensitivity, when retrieving  
454 L<sub>TCO</sub><sub>3</sub>, is important for influencing long-term tendencies, even when a more substantial trend is forced upon  
455 UKESM1.0. Future work on this would probably need to look at artificial model data which already has  
456 substantial T<sub>O</sub><sub>3</sub> trends in it (e.g. 5.0 or 10.0 DU/decade). This will obviously not match reality but would  
457 provide some further quantification on how important vertical sensitivity is from different  
458 instruments/sounders in L<sub>TO</sub><sub>3</sub> trend determination.

459 As for year-to-year sampling, our results suggest negligible trends for the product L<sub>TCO</sub><sub>3</sub> a priori time-series  
460 and thus monthly sampling biases are unlikely to be introducing artificial trends as the a priori datasets are  
461 trendless. Finally, the time-period over which the trend analysis is undertaken is critically important. Gaudel  
462 et al., (2018), using the available data at the time, focussed on 2005-2015/6 and 2008-2015/6 for the OMI  
463 and IASI products they used. For the IASI products, using a slightly extended time-period, the trends show  
464 similar tendencies. However, for OMI, 2016 and 2017 represent lower years of T<sub>O</sub><sub>3</sub>. As a result, this dampens  
465 the strong significant positive trends reported by Gaudel et al., (2018) in T<sub>CO</sub><sub>3</sub>. It is notable that the  
466 substantial positive increase in tropical L<sub>TO</sub><sub>3</sub> between 1995 and 2017 reported by Pope et al., (2023) from a  
467 series of UV-Vis sounders, included the same OMI global dataset as that is used here, further suggests the



468 selection of time period and geographical region to be crucial in regard to the role of interannual variability  
469 on linear trend detection.

## 470 5. Conclusions

471 Gaudel et al., (2018) undertook a multi-satellite analysis of long-term trends in tropospheric column ozone  
472 ( $\text{TCO}_3$ ). They found large scale differences between these products with no clear consensus on the signs or  
473 drivers of these  $\text{TCO}_3$  trends. To avoid complications with tropopause definition and reduce influence of  
474 stratospheric ozone on retrieved values, this study has undertaken a detailed follow-up assessment of  
475 decadal trends in  $\text{LTCO}_3$  (surface – 450 hPa layer) rather than  $\text{TCO}_3$  exploiting ozonesonde records, model  
476 simulations and accounting carefully for satellite  $\text{O}_3$  metrics (e.g. averaging kernels, AKs, apriori information  
477 and satellite uncertainties). We have focussed on  $\text{LTCO}_3$  data sets from Ozone Monitoring Instrument (OMI)  
478 produced by the RAL Space scheme and from Infrared Atmospheric Sounding Interferometer produced by  
479 the IASI-FORLI and IASI-SOFRID schemes, for which there were consistent records from 2008-2017.

480 Evaluation of satellite  $\text{LTO}_3$  from these three products over the North American, European and East Asian  
481 regions resulted in linear trends which varied over a small range close to zero and with confidence intervals  
482 intersecting with zero. This was consistent with simulations from the UK Earth System Model (UKESM1.0).  
483 There were no large-scale trends in the apriori information, so changes in satellite year-to-year sampling has  
484 not been driving inconsistencies between products. When convolving UKESM1.0 with the satellite AKs (i.e. to  
485 assess the impact of the satellite vertical sensitivity) it did change the size of the model trend, and in some  
486 instances, the direction of the trend, but as the simulated  $\text{LTO}_3$  trends were small and insignificant, they had  
487 limited influence. Overall, our results show that changes in  $\text{LTO}_3$  during the decade 2008-2017 in North  
488 America, Europe and East Asia were dominated by variability in processes which control  $\text{LTO}_3$  on shorter  
489 timescales.

490 In the future, new polar orbiting missions including the IASI Next Generation and Sentinel-5 UV/VIS sounders  
491 on the MetOp Second Generation will provide tropospheric ozone products to extend current missions  
492 through to the mid-2040s. There will also be the new geostationary platforms like the Infrared Sounder (IRS)  
493 and Sentinel 4 UV/VIS sounder on Meteosat-Third Generation (MTG-S) and the already in orbit  
494 Geostationary Environment Monitoring Spectrometer (GEMS) and Tropospheric Emissions: Monitoring of  
495 Pollution (TEMPO), which will provide large volumes of data (e.g. diurnal observations) and over a long-time  
496 scale on tropospheric ozone for future regional trend analyses.

## 497 Acknowledgements

498 This work was funded by the UK Natural Environment Research Council (NERC) by providing funding for the  
499 National Centre for Earth Observation (NCEO, award reference NE/R016518/1) and funding from the  
500 European Space Agency (ESA) Climate Change Initiative (CCI) post-doctoral fellowship scheme (award  
501 reference 4000137140). For UKESM1.0 model runs, we acknowledge use of the Monsoon2 system, a  
502 collaborative facility supplied under the Joint Weather and Climate Research Programme, a strategic  
503 partnership between the Met Office and NERC. IASI is a joint mission of EUMETSAT and the Centre National  
504 d'Etudes Spatiales (CNES, France). The IASI-SOFRID research was conducted at LAERO with some financial  
505 support from the CNES French spatial agency (TOSCA-IASI project). The authors acknowledge the AERIS data  
506 infrastructure for providing access to the IASI-FORLI data, ULB-LATMOS for the development of the FORLI  
507 retrieval algorithm, and the AC SAF project of the EUMETSAT for providing IASI-FORLI data used in this  
508 paper. Anna Maria Trofaier (ESA Climate Office) provided support and advice throughout the fellowship.

509

510



#### 511 **Data Availability**

512 The IASI-FORLI and IASI-SOFRID data can be obtained from <https://iasi.aeris-data.fr/O3> and <https://iasi-sofrid.sedoo.fr/>. The RAL OMI data is available via the NERC Centre for Environmental Data Analysis (CEDA)  
513 Jasmin platform subject to data requests. However, the RAL Space satellite data, as well as the UKESM1.0  
514 simulations, will be uploaded to the Zenodo open access portal (<https://zenodo.org/>) if this manuscript is  
515 accepted for publication in ACP after the peer-review process. The ozonesonde data for WOUDC, SHADOZ  
516 and NOAA is available from <https://woudc.org/>, <https://tropo.gsfc.nasa.gov/shadoz/> and  
517 <https://gml.noaa.gov/ozwv/ozsondes/>.

#### 519 **Author Contributions**

520 RJP conceptualised, planned and undertook the research study. BB, ELF, BJK, RS, BGL, LJV, AB and CW  
521 provided the OMI and IASI ozone data and advice on using the products. FO and MD provided advice and  
522 expertise on using and running UKESM. CR provided advice and help during RP's ESA CCI fellowship. RJP  
523 prepared the manuscript with scientific and technical contributions from all co-authors.

#### 524 **Conflicts of Interest**

525 The authors declare no conflicts of interest.

#### 526 **References:**

- 527 Archibald, A.T., O'Connor, F.M., Abraham, N.L., Archer-Nicholls, S., Chipperfield, M.P., Dalvi, M., Folberth,  
528 G.A., Dennison, F., Dhomse, S.S., Griffiths, P.T., Hardacre, C., Hewitt, A.J., Hill, R.S., Johnson, C.E., Keeble, J.,  
529 Kohler, M.O., Morgenstern, O., Mulcahy, J.P., Ordonez, C., Pope, R.J., Rumbold, S.T., Russo, M.R., Savage,  
530 N.H., Sellar, A., Stringer, M., Turnock, S.T., Wild, O. and Zeng, G.: Description and evaluation of the UKCA  
531 stratosphere–troposphere chemistry scheme (StratTrop vn 1.0) implemented in UKESM1. *Geoscientific*  
532 *Model Development*, **13**, 1223–1266, doi: 10.5194/gmd-13-1223-2020, 2020.
- 533 Barret, B., Emili, E., Le Flochmoen, E. 2020. A tropopause-related climatological a priori profile for IASI-  
534 SOFRID ozone retrievals: improvements and validation. *Atmospheric Measurement Techniques*, **13**, 5237–  
535 5257, doi: 10.5194/amt-13-5237-2020.
- 536 Boersma, K.F., Jacob, D.J., Eskes, H.J., Pinder, R.W., Wang, J. and van der A, R.J.: Intercomparison of  
537 SCIAMACHY and OMI tropospheric NO<sub>2</sub> columns: Observing the diurnal evolution of chemistry and emissions  
538 from space. *Journal of Geophysical Research: Atmospheres*, **113** (D16S26), doi: 10.1029/2007JD008816,  
539 2008.
- 540 Boersma, K. F., Eskes, H. J., Dirksen, R. J., van der A, R. J., Veefkind, J. P., Stammes, P., Huijnen, V., Kleipool,  
541 Q. L., Sneep, M., Claas, J., Leitão, J., Richter, A., Zhou, Y., and Brunner, D.: An improved tropospheric  
542 NO<sub>2</sub> column retrieval algorithm for the Ozone Monitoring Instrument, *Atmospheric Measurement*  
543 *Techniques*, **4**, 1905–1928, doi: 10.5194/amt-4-1905-2011, 2011.
- 544 Boynard, A., Hurtmans, D., Garane, K., Goutail, F., Hadji-Lazaro, J., Koukouli, M. E., Wespes, C., Vigouroux, C.,  
545 Keppens, A., Pommereau, J.-P., Pazmino, A., Balis, D., Loyola, D., Valks, P., Sussmann, R., Smale, D., Coheur,  
546 P.-F., and Clerbaux, C.: Validation of the IASI FORLI/EUMETSAT ozone products using satellite (GOME-2),  
547 ground-based (Brewer–Dobson, SAOZ, FTIR) and ozonesonde measurements, *Atmospheric Measurement*  
548 *Techniques*, **11**, 5125–5152, <https://doi.org/10.5194/amt-11-5125-2018>, 2018.
- 549 Clerbaux, C., Boynard, A., Clarisse, L., George, M., Hadji-Lazaro, J., Herbin, H., Hurtmans, D., Pommier, M.,  
550 Razavi, A., Turquety, S., Wespes, C. and Coheur, P.F.: Monitoring of atmospheric composition using the



- 551 thermal infrared IASI/MetOp sounder, *Atmospheric Chemistry and Physics*, 9 (16), 6041–6054,  
552 doi:10.5194/acp-9-6041-2009, 2009.
- 553 Doherty, R. M., Heal, M. R., and O'Connor, F. M.: Climate change impacts on human health over Europe  
554 through its effect on air quality, *Environmental Health*, 16(1), 33–44, doi:10.1186/s12940-017-0325-2, 2017.
- 555 ESA. 2019. Climate Change Initiative. <http://cci.esa.int/ozone> (last accessed 01/09/2022).
- 556 Eskes HJ and Boersma KF. 2003. Averaging kernels for DOAS total column satellite retrievals. *Atmospheric*  
557 *Chemistry and Physics*, 3, 1285–1291, doi: 10.5194/acp-3-1285-2003.
- 558 European Commission, Joint Research Centre, Dentener F, et al. 2016. Hemispheric Transport of Air Pollution  
559 (HTAP): specification of the HTAP2 experiments: ensuring harmonized modelling, Publications Office,  
560 <https://data.europa.eu/doi/10.2788/725244>.
- 561 Eyring, V., Bony, S., Meehl, G. A., Senior, C. A., Stevens, B., Stouffer, R. J., and Taylor, K. E.: Overview of the  
562 Coupled Model Intercomparison Project Phase 6 (CMIP6) experimental design and organization, *Geosci.*  
563 *Model Dev.*, 9, 1937–1958, <https://doi.org/10.5194/gmd-9-1937-2016>, 2016. Gaudel A, et al. 2018.  
564 Tropospheric Ozone Assessment Report: Present day distribution and trends of tropospheric ozone relevant  
565 to climate and global atmospheric chemistry model evaluation. *Elementa*, 6 (39), 1-58, doi:  
566 10.1525/elementa.291.
- 567 Forster, P., Storelvmo, T., Armour, K., Collins, W., Dufresne, J.-L., Frame, D., Lunt, D. J., Mauritsen, T.,  
568 Palmer, M. D., Watanabe, M., Wild, M., and Zhang, H.: The Earth's Energy Budget, Climate Feedbacks, and  
569 Climate Sensitivity, in: *Climate Change 2021: The Physical Science Basis, Contribution of Working Group I to*  
570 *the Sixth Assessment Report of the Intergovernmental Panel on Climate Change*, edited by: Masson-  
571 Delmotte, V., Zhai, P., Pirani, A., Connors, S. L., Péan, C., Berger, S., Caud, N., Chen, Y., Goldfarb, L., Gomis, M.  
572 I., Huang, M., Leitzell, K., Lonnoy, E., Matthews, J. B. R., Maycock, T. K., Waterfield, T., Yelekçi, O., Yu, R., and  
573 Zhou, B., Cambridge University Press, Cambridge, United Kingdom and New York, NY, USA, 923–1054,  
574 doi:10.1017/9781009157896.009, 2021.
- 575 Gaudel, A., Cooper, O.R., Ancellet, G., Barret, B., Boynard, A., Burrows, J.P., Clerbaux, C., Coheur, P.F.,  
576 Cuesta, J., Cuevas, E., Doniki, S., Dufour, G., Ebojic, F., Foret, G., Garia, O., Granados-Munoz, M.J., Hannigan,  
577 J.W., Hase, F., Hassler, B., Huang, G., Hurtmans, D., Jaffe, D., Jones, N., Kalabokas, P., Kerridge, B., Kulwaik, S.,  
578 Latter, B., Leblanc, T., Le Flochmoen, E., Lin, W., Liu, J., Liu, X., Mahieu, E., McClure-Begley, A., Neu, J.L.,  
579 Osman, M., Palm, M., Petetin, H., Petropavlovskikh, I., Querel, R., Rapp, N., Rozanov, A., Schultz, M.G.,  
580 Schwab, J., Siddans, R., Smale, D., Steinbacher, M., Tanimoto, H., Tarasick, D.W., Thouret, V., Thompson,  
581 A.M., Trickl, T., Weatherhead, E., Wespes, C., Worden, H.M., Vigouroux, C., Xu, X., Zeng, G. and Ziemke, J.:  
582 Tropospheric Ozone Assessment Report: Present day distribution and trends of tropospheric ozone relevant  
583 to climate and global atmospheric chemistry model evaluation. *Elementa*, 6(39), 1-58,  
584 doi:10.1525/elementa.291, 2018.
- 585 Gauss, M., Myhre, G., Isaksen, I. S. A., Grewe, V., Pitari, G., Wild, O., Collins, W. J., Dentener, F. J., Ellingsen,  
586 K., Gohar, L. K., Hauglustaine, D. A., Iachetti, D., Lamarque, F., Mancini, E., Mickley, L. J., Prather, M. J., Pyle,  
587 J. A., Sanderson, M. G., Shine, K. P., Stevenson, D. S., Sudo, K., Szopa, S., and Zeng, G.: Radiative forcing since  
588 preindustrial times due to ozone change in the troposphere and the lower stratosphere, *Atmospheric*  
589 *Chemistry and Physics*, 6, 575–599, <https://doi.org/10.5194/acp-6-575-2006>, 2006.
- 590 Hoesly, R. M., Smith, S. J., Feng, L., Klimont, Z., Janssens-Maenhout, G., Pitkanen, T., Seibert, J. J., Vu, L.,  
591 Andres, R. J., Bolt, R. M., Bond, T. C., Dawidowski, L., Kholod, N., Kurokawa, J.-I., Li, M., Liu, L., Lu, Z., Moura,





- 592 M. C. P., O'Rourke, P. R., and Zhang, Q.: Historical (1750–2014) anthropogenic emissions of reactive gases  
593 and aerosols from the Community Emissions Data System (CEDS), *Geoscientific Model Development*, **11**,  
594 369–408, <https://doi.org/10.5194/gmd-11-369-2018>, 2018.
- 595 Hollaway, M.J., Arnold, S.R., Challinor, A. J. and Emberson, L.D: Intercontinental trans-boundary  
596 contributions to ozone-induced crop yield losses in the North Hemisphere, *Biogeosciences*, **9**, 271–2929, doi:  
597 10.5194/bg-9-271-2012, 2012.
- 598 Illingworth, S. M., Remedios, J. J., Boesch, H., Moore, D. P., Sembhi, H., Dudhia, A., and Walker, J. C.: ULIRS,  
599 an optimal estimation retrieval scheme for carbon monoxide using IASI spectral radiances: sensitivity  
600 analysis, error budget and simulations, *Atmospheric Measurements Techniques*, **4**, 269–288, doi:  
601 10.5194/amt-4-269-2011, 2011.
- 602 Keim, C., Eremenko, M., Orphal, J., Dufour, G., Flaud, J.-M., Höpfner, M., Boynard, A., Clerbaux, C., Payan, S.,  
603 Coheur, P.-F., Hurtmans, D., Claude, H., Dier, H., Johnson, B., Kelder, H., Kivi, R., Koide, T., López Bartolomé,  
604 M., Lambkin, K., Moore, D., Schmidlin, F. J., and Stübi, R.: Tropospheric ozone from IASI: comparison of  
605 different inversion algorithms and validation with ozone sondes in the northern middle latitudes,  
606 *Atmospheric Chemistry and Physics*, **9**, 9329–9347, doi: 10.5194/acp-9-9329-2009, 2009.
- 607 Lamarque, J.-F., Bond, T. C., Eyring, V., Granier, C., Heil, A., Klimont, Z., Lee, D., Liousse, C., Mieville, A.,  
608 Owen, B., Schultz, M. G., Shindell, D., Smith, S. J., Stehfest, E., Van Aardenne, J., Cooper, O. R., Kainuma, M.,  
609 Mahowald, N., McConnell, J. R., Naik, V., Riahi, K., and van Vuuren, D. P.: Historical (1850–2000) gridded  
610 anthropogenic and biomass burning emissions of reactive gases and aerosols: methodology and application,  
611 *Atmospheric Chemistry and Physics*, **10**, 7017–7039, doi: 10.5194/acp-10-7017-2010, 2010.
- 612 Matthes, K., Funke, B., Andersson, M. E., Barnard, L., Beer, J., Charbonneau, P., Clilverd, M. A., Dudok de Wit,  
613 T., Haberreiter, M., Hendry, A., Jackman, C. H., Kretschmar, M., Kruschke, T., Kunze, M., Langematz, U.,  
614 Marsh, D. R., Maycock, A. C., Misios, S., Rodger, C. J., Scaife, A. A., Seppälä, A., Shangguan, M., Sinnhuber,  
615 M., Tourpali, K., Usoskin, I., van de Kamp, M., Verronen, P. T., and Versick, S.: Solar forcing for CMIP6 (v3.2),  
616 *Geoscientific Model Development*, **10**, 2247–2302, <https://doi.org/10.5194/gmd-10-2247-2017>, 2017.
- 617 McPeters, R.D., Labow, G.J., and Logan, J.A. 2007. Ozone climatological profiles for satellite retrieval  
618 algorithms. *Journal of Geophysical Research*, **112** (D05308), <https://doi.org/10.1029/2005JD006823>.
- 619 Miles, G.M., Siddans, R., Kerridge, B. J., Latter, B. G., and Richards, N. A. D.: Tropospheric ozone and ozone  
620 profiles retrieved from GOME-2 and their validation, *Atmospheric Measurement Techniques*, **8**, 385–398,  
621 doi:10.5194/amt-8-385-2015, 2015.
- 622 Monks, S.A., Arnold, S.R., Hollaway, M. J., Pope, R.J., Wilson, C., Feng, W., Emmerson, K.E., Kerridge, B.J.,  
623 Latter, B.L., Miles, G.M., Siddans, R. and Chipperfield, M.P.: The TOMCAT global chemistry transport model  
624 v1.6: Description of chemical mechanism and model evaluation, *Geoscientific Model Development*, **10** (8),  
625 3025–3057, doi:10.5194/gmd-10-3025-2017, 2017.
- 626 Myhre, G., Shindell, D., Bréon, F.-M, Collins, W., Fuglestedt, J., Huang, J., Koch, D., Lamarque, J.-F., Lee, D.,  
627 Mendoza, B., Nakajima, T., Robock, A., Stephens, G., Takemura, T. and Zhang, H.: Anthropogenic and Natural  
628 Radiative Forcing, in: *Climate Change 2013: The Physical Science Basis. Contribution of Working Group I to  
629 the Fifth Assessment Report of the Intergovernmental Panel on Climate Change*, Cambridge University Press,  
630 Cambridge, United Kingdom and New York, NY, USA, 659–740, 2013.
- 631 O'Connor, F. M., Johnson, C. E., Morgenstern, O., Abraham, N. L., Braesicke, P., Dalvi, M., Folberth, G. A.,  
632 Sanderson, M. G., Telford, P. J., Voulgarakis, A., Young, P. J., Zeng, G., Collins, W. J., and Pyle, J. A.: Evaluation



- 633 of the new UKCA climate-composition model – Part 2: The Troposphere, *Geoscientific Model Development*,  
634 7, 41–91, doi: 10.5194/gmd-7-41-2014, 2014.
- 635 Pimlott, M.A., Pope, R.P., Kerridge, B.J., Latter, B.G., Knappett, D.S., Heard, D.E., Ventress, L.J., Siddans, R.,  
636 Feng, W. and Chipperfield, M.P.: Investigating the global OH radical distribution using steady-state  
637 approximations and satellite data. *Atmospheric Chemistry and Physics*, **22**, 10467–10488, doi: 10.5194/acp-  
638 22-10467-2022, 2022.
- 639 Pope, R.J., Arnold, S.R., Chipperfield, M.P., Latter, B.G., Siddans, R. and Kerridge, B.J.: Widespread changes in  
640 UK air quality observed from space. *Atmospheric Science Letters*, **19**:e817, doi: 10.1002/asl.817.
- 641 Pope, R. J., Kerridge, B. J., Siddans, R., Latter, B. G., Chipperfield, M. P., Feng, W., Pimlott, M. A., Dhomse, S.  
642 S., Retscher, C., and Rigby, R.: Investigation of spatial and temporal variability in lower tropospheric ozone  
643 from RAL Space UV–Vis satellite products, *Atmospheric Chemistry and Physics*, **23**, 14933–14947,  
644 <https://doi.org/10.5194/acp-23-14933-2023>, 2023.
- 645 Rao, S., Klimont, Z., Smith, S.J., Van Dingenen, R., Dentener, F., Bouwman, L., Riahi, K., Amann, M., Bodirsky,  
646 B.L., van Vuuren, D.P., Reus, L.R., Calvin, K., Drouet, L., Fricko, O., Fujimori, S., Gernaat, D., Havlik, P.,  
647 Harmsen, M., Hasegawa, T., Heyes, C. and Tavoni, M.: Future air pollution in the shared socio-economic  
648 pathways. *Global Environmental Change*, **42**, 346–358, doi: 10.1016/j.gloenvcha.2016.05.012.
- 649 Richards, N.A.D, Osterman, G.B., Browell, E.V., Hair, J.W., Avery, M. and Li, Q.: Validation of tropospheric  
650 emission spectrometer ozone profiles with aircraft observations during the intercontinental chemical  
651 transport experiment–B. *Journal Geophysical Research*, **113**(D16S29), doi: 10.1029/2007JD008815, 2008.
- 652 Sellar, A.A., Jones, C.G., Mulcahy, J.P., Tang, Y., Yool, A., Wiltshire, A., O’Connor, F.M., Stringer, M., Hill, R.,  
653 Palmieri, J., Woodward, S., de Mora, L., Kuhlbrodt, T., Rumbold, S.T., Kelley, D.I., Ellis, R., John, C.E., Walton,  
654 J., Abraham, N.L., Andrews, M.B., Andrews, T., Archibald, A.T., Berthou, S., Burke, E., Blockley, E., Carslaw, K.,  
655 Dalvi, M., Edwards, J., Folbert, G.A., Gedney, N., Griffiths, P.T., Harper, A.B., Hendry, M.A., Hewitt, A.J.,  
656 Johnson, B., Jones, A., Jones, C.D., Keebie, J., Liddicoat, S., Morgenstern, O., Parker, R.J., Predoi, V.,  
657 Robertson, E., Siahann, A., Smith, R.S., Swaminathan, R., Woodhouse, M.T., Zeng, G. and Zerroukat, M.:  
658 Description and Evaluation of the UK Earth System Model. *Journal of Advances in Modeling Earth Systems*,  
659 **11**, 4513–4558, doi: 10.1029/2019MS001739, 2019.
- 660 Sindelarova, K., Granier, C., Bouarar, I., Guenther, A., Tilmes, S., Stavrakou, T., Müller, J.-F., Kuhn, U., Stefani,  
661 P., and Knorr, W.: Global data set of biogenic VOC emissions calculated by the MEGAN model over the last  
662 30 years, *Atmos. Chem. Phys.*, **14**, 9317–9341, doi: 10.5194/acp-14-9317-2014, 2014.
- 663 Sitch, S., Cox, P.M., Collins, W.J., & Huntingford, C.: Indirect radiative forcing of climate change through  
664 ozone effects on the land carbon sink, *Nature*, **448**, 791–795, doi:10.1038/nature06059, 2007.
- 665 Telford, P. J., Braesicke, P., Morgenstern, O., and Pyle, J. A.: Technical Note: Description and assessment of a  
666 nudged version of the new dynamics Unified Model, *Atmospheric Chemistry and Physics*, **8**, 1701–1712,  
667 <https://doi.org/10.5194/acp-8-1701-2008>, 2008.
- 668 van der A, R.J., Peters, D.H.M.U., Eskes, H., Boersma, K.F., Van Roozendaal, M., De Smedt, I. and Kelder,  
669 H.M.: Detection of the trend and seasonal variation in tropospheric NO<sub>2</sub> over China. *Journal of Geophysical*  
670 *Research*, **11**, D12317, doi: 10.1029/2005JD006594, 2006.
- 671 van der A, R.J., Eskes, H.J., Boersma, K.F., van Noije, T.P.C., Van Roozendaal, M., De Smedt, I., Peters,  
672 D.H.M.U. and Meijer, E.W.: Trends, seasonal variability and dominant NO<sub>x</sub> sources derived from a ten year



- 673 record of NO<sub>2</sub> measured from space. *Journal of Geophysical Research*, **113**, 1–12, doi:  
674 10.1029/2007JD009021, 2008.
- 675 van der Werf, G. R., Randerson, J. T., Giglio, L., van Leeuwen, T. T., Chen, Y., Rogers, B. M., Mu, M., van  
676 Marle, M. J. E., Morton, D. C., Collatz, G. J., Yokelson, R. J., and Kasibhatla, P. S.: Global fire emissions  
677 estimates during 1997–2016, *Earth System Science Data*, 9, 697–720, [https://doi.org/10.5194/essd-9-697-](https://doi.org/10.5194/essd-9-697-2017)  
678 2017, 2017.
- 679 van Marle, M. J. E., Kloster, S., Magi, B. I., Marlon, J. R., Daniau, A.-L., Field, R. D., Arneeth, A., Forrest, M.,  
680 Hantson, S., Kehrwald, N. M., Knorr, W., Lasslop, G., Li, F., Mangeon, S., Yue, C., Kaiser, J. W., and van der  
681 Werf, G. R.: Historic global biomass burning emissions for CMIP6 (BB4CMIP) based on merging satellite  
682 observations with proxies and fire models (1750–2015), *Geoscientific Model Development*, 10, 3329–3357,  
683 <https://doi.org/10.5194/gmd-10-3329-2017>, 2017.
- 684 Weatherhead, E.C., Reinsel, G.C., Tiao, G.C., Meng, X., Choi, D., Cheang, W., Keller, T., De Luisi, J., Wuebbles,  
685 D.J., Kerr, J.B., Miller, A.J., Oltmans, S.J. and Frederick, J.E.: Factors affecting the detection of trends:  
686 statistical considerations and applications to environmental data. *Journal of Geophysical Research*, **103(D14)**,  
687 17149–17161, doi: 10.1029/98JD00995, 1998.
- 688 Wespes, C., Hurtmans, D., Clerbaux, C., Boynard, A., and Coheur, P.-F. 2018. Decrease in tropospheric O<sub>3</sub>  
689 levels in the Northern Hemisphere observed by IASI. *Atmospheric Chemistry and Physics*, **18**, 6867–6885,  
690 doi:10.5194/acp-18-6867-2018.
- 691 WHO (World Health Organisation), Ambient (outdoor) air pollution, available at: [https://www.who.int/news-](https://www.who.int/news-room/fact-sheets/detail/ambient-(outdoor)-air-quality-and-health)  
692 room/fact-sheets/detail/ambient-(outdoor)-air-quality-and-health (last accessed 2<sup>nd</sup> January 2024), 2022.
- 693 Wiltshire, A.J., Burke, E.J., Chadburn, S.E., Jones, C.D., Cox, P.M., Davies-Barnard, T., Friedlingstein, P.,  
694 Harper, A.B., Liddicoat, S., Sitch, S. and Zaehle, S.: JULES-CN: a coupled terrestrial carbon–nitrogen scheme  
695 (JULES vn5.1). *Geophysical Model Development*, 14 (4), 2161–2186, doi: 10.5194/gmd-14-2161-2021,  
696 2021. Yool A, et al. 2013. MEDUSA-2.0: an intermediate complexity biogeochemical model of the marine  
697 carbon cycle for climate change and ocean acidification studies. *Geoscientific Model Development*, **6**, 1767–  
698 1811, doi: 10.5194/gmd-6-1767-2013.
- 699 Young, P.J., Archibald, A.T., Bowman, K.W., Lamarque, J.-F., Naik, V., Stevenson, D.S., Tilmes, S., Voulgarakis,  
700 A., Wild, O., Bergmann, D., Cameron-Smith, P., Cionni, I., Collins, W.J., Dalsoren, S.B., Doherty, R.M., Eyring,  
701 V., Faluvegi, G., Horowitz, L.W., Josse, B., Lee, Y.H., MacKenzie, I.A., Nagashima, T., Plummer, D.A., Righi, M.,  
702 Rumbold, S.T., Skeie, R.B., Shindell, D.T., Strode, S.A., Sudo, K., Szopa, S. and Zeng, G.: Pre-industrial to end  
703 21st century projections of tropospheric ozone from the Atmospheric Chemistry and Climate Model  
704 Intercomparison Project (ACCMIP). *Atmospheric Chemistry and Physics*, 13, 2063–2090, doi: 10.5194/acp-13-  
705 2063-2013, 2013.
- 706 Ziemke, J.R., Chandra, S., Labow, G.J., Bhartia, P.K., Froidevaux, L. and Witte, J.C.: A global climatology of  
707 tropospheric and stratospheric ozone derived from Aura OMI/MLS measurements, *Atmospheric Chemistry*  
708 *and Physics*, 11, 9237–9251, doi: /10.5194/acp-11-9237-2011, 2011.
- 709
- 710
- 711
- 712



713 **Figures & Tables:**

714

| Data Provider             | Satellite Profile<br>Products & Version | Product Link  | Data<br>Range | Data Size |
|---------------------------|---|---|---------------|-----------|
| RAL Space                 | OMI-fv214                               | <a href="http://www.ceda.ac.uk/">http://www.ceda.ac.uk/</a>                           | 2004-2018     | 1442 GB   |
| ATMOS-ULB                 | IAS-FORLI-v20151001                     | <a href="https://iasi.aeris-data.fr/catalog/">https://iasi.aeris-data.fr/catalog/</a> | 2008-2019     | 9.1 TB    |
| Université de<br>Toulouse | IASI-SOFRID vn3.5                       | <a href="https://iasi-sofrid.sedoo.fr/">https://iasi-sofrid.sedoo.fr/</a>             | 2008-2017     | 3.0 TB    |

715

716

**Table 1:** List of the satellite ozone profile data sets.

717

| Satellite | Quantity               | Trend | Trend Lower | Trend Upper | p-value | Fit (R <sup>2</sup> ) |
|-----------|------------------------|-------|-------------|-------------|---------|-----------------------|
| OMI       | Trend                  | -0.79 | -7.07       | 5.48        | 0.80    | 0.58                  |
|           | Trend Error 1          | -1.50 | -7.04       | 4.04        | 0.59    | 0.68                  |
|           | Trend Error 2          | -0.09 | -6.98       | 6.81        | 0.98    | 0.50                  |
|           | Apriori Trend          | -0.05 | -0.21       | 0.11        | 0.56    | 1.00                  |
|           | UKESM Trend            | 0.21  | -0.37       | 0.78        | 0.47    | 0.95                  |
|           | UKESM+AKs Trend        | -0.57 | -1.58       | 0.45        | 0.26    | 0.90                  |
|           | UKESM Trend Forced     | 0.73  | 0.22        | 1.25        | 0.00    | 0.95                  |
|           | UKESM+AKs Trend Forced | -0.74 | -1.89       | 0.40        | 0.20    | 0.89                  |
| FORLI     | Trend                  | -1.42 | -2.35       | -0.50       | 0.00    | 0.93                  |
|           | Trend Error 1          | -1.34 | -2.21       | -0.47       | 0.00    | 0.93                  |
|           | Trend Error 2          | -1.50 | -2.51       | -0.50       | 0.00    | 0.93                  |
|           | Apriori Trend          | 0.00  | -0.11       | 0.12        | 0.94    | 0.67                  |
|           | UKESM Trend            | -0.13 | -0.75       | 0.49        | 0.67    | 0.93                  |
|           | UKESM+AKs Trend        | -0.32 | -0.83       | 0.20        | 0.22    | 0.92                  |
|           | UKESM Trend Forced     | 0.64  | -3.50       | 4.77        | 0.76    | 0.46                  |
|           | UKESM+AKs Trend Forced | 0.55  | 0.08        | 1.03        | 0.02    | 0.93                  |
| SOFRID    | Trend                  | 0.12  | -0.59       | 0.82        | 0.74    | 0.94                  |
|           | Trend Error 1          | 0.14  | -0.59       | 0.88        | 0.70    | 0.90                  |
|           | Trend Error 2          | 0.09  | -0.48       | 0.66        | 0.75    | 0.94                  |
|           | Apriori Trend          | 0.11  | -0.17       | 0.39        | 0.43    | 0.98                  |
|           | UKESM Trend            | -0.24 | -0.85       | 0.37        | 0.44    | 0.95                  |
|           | UKESM+AKs Trend        | -0.04 | -0.53       | 0.45        | 0.87    | 0.97                  |
|           | UKESM Trend Forced     | 0.80  | 0.41        | 1.19        | 0.00    | 0.97                  |
|           | UKESM+AKs Trend Forced | 0.58  | 0.24        | 0.92        | 0.00    | 0.98                  |
| OMI       | Trend                  | -0.80 | -7.29       | 5.69        | 0.80    | 0.71                  |
|           | Trend Error 1          | -1.65 | -6.92       | 3.62        | 0.53    | 0.76                  |
|           | Trend Error 2          | 0.05  | -7.44       | 7.53        | 0.99    | 0.67                  |
|           | Apriori Trend          | -0.12 | -0.26       | 0.03        | 0.10    | 1.00                  |
|           | UKESM Trend            | -0.11 | -0.50       | 0.29        | 0.59    | 0.99                  |
|           | UKESM+AKs Trend        | -0.72 | -1.77       | 0.32        | 0.16    | 0.95                  |
|           | UKESM Trend Forced     | 0.62  | 0.14        | 1.10        | 0.01    | 0.98                  |
|           | UKESM+AKs Trend Forced | 0.47  | -0.51       | 1.44        | 0.34    | 0.94                  |



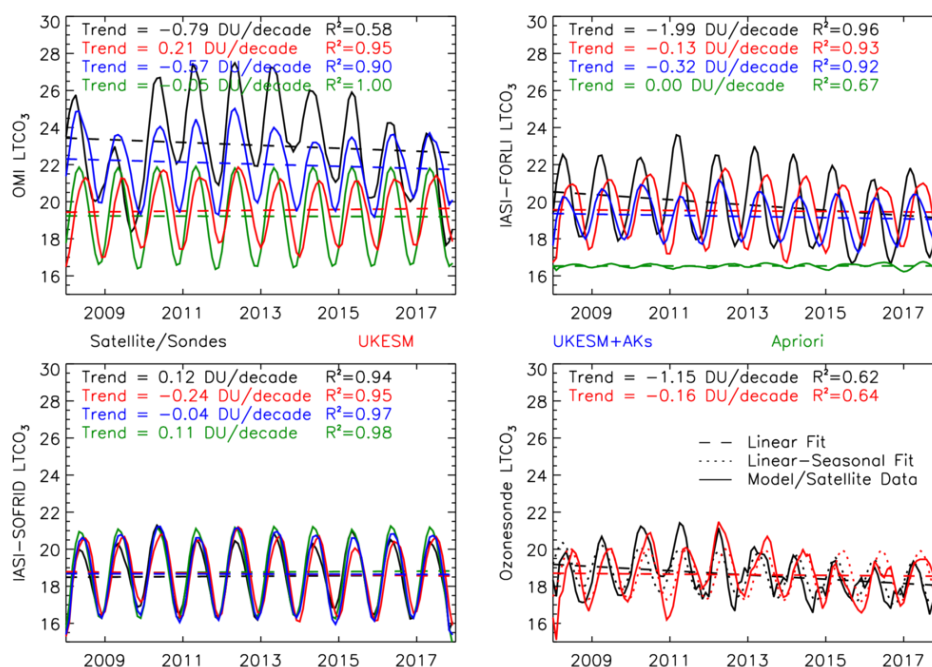
|        |                        |       |       |       |      |      |
|--------|------------------------|-------|-------|-------|------|------|
| FORLI  | Trend                  | -1.83 | -2.78 | -0.89 | 0.00 | 0.92 |
|        | Trend Error 1          | -1.80 | -2.72 | -0.88 | 0.00 | 0.93 |
|        | Trend Error 2          | -1.87 | -2.87 | -0.87 | 0.00 | 0.92 |
|        | Apriori Trend          | 0.09  | -0.09 | 0.27  | 0.32 | 0.48 |
|        | UKESM Trend            | -0.28 | -0.77 | 0.20  | 0.25 | 0.98 |
|        | UKESM+AKs Trend        | -0.43 | -1.21 | 0.35  | 0.27 | 0.94 |
|        | UKESM Trend Forced     | 0.37  | -0.05 | 0.79  | 0.08 | 0.98 |
|        | UKESM+AKs Trend Forced | 0.28  | -0.38 | 0.94  | 0.40 | 0.93 |
| SOFRID | Trend                  | 0.05  | -0.91 | 1.01  | 0.92 | 0.93 |
|        | Trend Error 1          | 0.16  | -0.74 | 1.07  | 0.72 | 0.91 |
|        | Trend Error 2          | -0.07 | -0.91 | 0.78  | 0.87 | 0.93 |
|        | Apriori Trend          | 0.17  | -0.12 | 0.45  | 0.24 | 0.98 |
|        | UKESM Trend            | -0.27 | -0.72 | 0.19  | 0.24 | 0.98 |
|        | UKESM+AKs Trend        | 0.08  | -0.33 | 0.49  | 0.69 | 0.98 |
|        | UKESM Trend Forced     | 0.46  | 0.09  | 0.84  | 0.01 | 0.99 |
|        | UKESM+AKs Trend Forced | 0.10  | -0.32 | 0.51  | 0.64 | 0.98 |
| OMI    | Trend                  | -0.09 | -7.88 | 7.70  | 0.98 | 0.51 |
|        | Trend Error 1          | -1.05 | -6.61 | 4.52  | 0.70 | 0.66 |
|        | Trend Error 2          | 0.87  | -8.24 | 9.98  | 0.85 | 0.38 |
|        | Apriori Trend          | -0.25 | -0.71 | 0.22  | 0.29 | 0.98 |
|        | UKESM Trend            | -0.16 | -0.94 | 0.62  | 0.67 | 0.98 |
|        | UKESM+AKs Trend        | -0.62 | -2.24 | 1.00  | 0.44 | 0.95 |
|        | UKESM Trend Forced     | 0.90  | 0.34  | 1.47  | 0.00 | 0.99 |
|        | UKESM+AKs Trend Forced | 1.02  | -0.04 | 2.09  | 0.05 | 0.97 |
| FORLI  | Trend                  | -1.52 | -2.16 | -0.88 | 0.00 | 0.93 |
|        | Trend Error 1          | -1.42 | -2.06 | -0.78 | 0.00 | 0.93 |
|        | Trend Error 2          | -1.62 | -2.27 | -0.98 | 0.00 | 0.92 |
|        | Apriori Trend          | -0.03 | -0.22 | 0.16  | 0.76 | 0.21 |
|        | UKESM Trend            | -0.03 | -0.62 | 0.56  | 0.93 | 0.98 |
|        | UKESM+AKs Trend        | -0.29 | -0.80 | 0.22  | 0.25 | 0.95 |
|        | UKESM Trend Forced     | 0.66  | 0.15  | 1.17  | 0.01 | 0.98 |
|        | UKESM+AKs Trend Forced | 0.08  | -0.44 | 0.61  | 0.75 | 0.93 |
| SOFRID | Trend                  | -0.19 | -1.01 | 0.63  | 0.65 | 0.96 |
|        | Trend Error 1          | -0.08 | -0.73 | 0.58  | 0.82 | 0.90 |
|        | Trend Error 2          | -0.30 | -1.02 | 0.42  | 0.41 | 0.93 |
|        | Apriori Trend          | -0.15 | -0.39 | 0.09  | 0.21 | 0.98 |
|        | UKESM Trend            | -0.42 | -0.97 | 0.13  | 0.12 | 0.99 |
|        | UKESM+AKs Trend        | -0.24 | -0.67 | 0.20  | 0.28 | 0.98 |
|        | UKESM Trend Forced     | 0.63  | 0.26  | 1.00  | 0.00 | 0.99 |
|        | UKESM+AKs Trend Forced | 0.20  | -0.20 | 0.61  | 0.31 | 0.98 |

718

719 **Table 2:** *LTCO<sub>3</sub> trends (DU/decade) for the satellite trend (Trend), the satellite-uncertainty trend (Trend Error*  
 720 *1), the satellite+uncertainty trend (Trend Error 2), the satellite apriori trend (Apriori Trend), UKESM trend*  
 721 *(UKESM Trend), UKESM with AKs applied trend (UKESM+AKs Trend), UKESM forced trend (UKESM Trend*  
 722 *Forced) and UKESM with AKs applied forced trend (UKESM+AKs Trend Forced). The trends from OMI, IASI-*

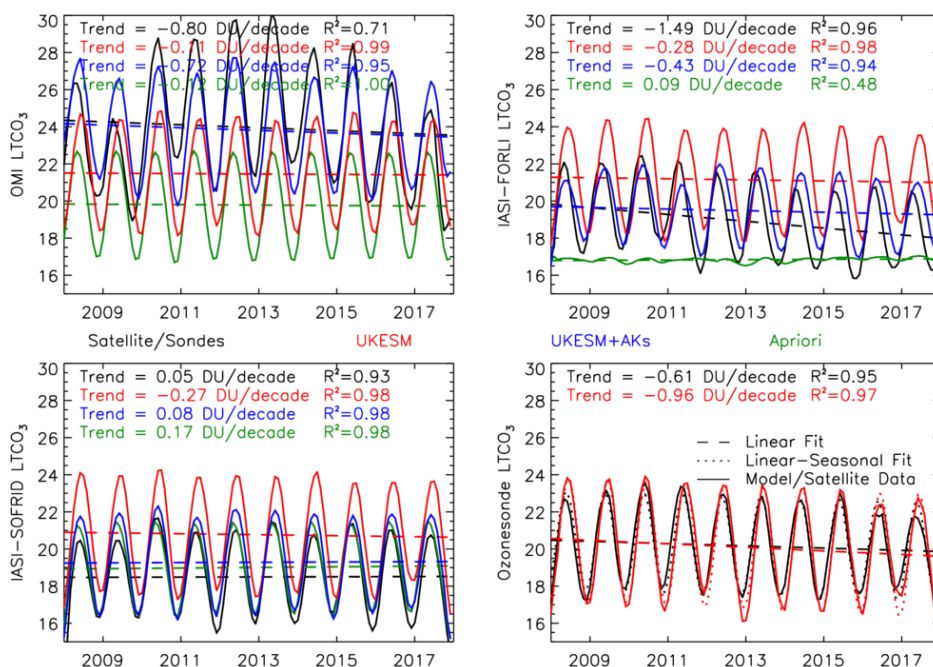


723 FORLI and IASI-SOFRID are for North America (red), Europe (blue) and East Asia (green). The trend lower and  
 724 trend upper represent the trend 95% confidence interval.  $R^2$  is the trend fit skill (i.e. correlation squared) and  
 725 the p-value is also shown.  
 726  
 727



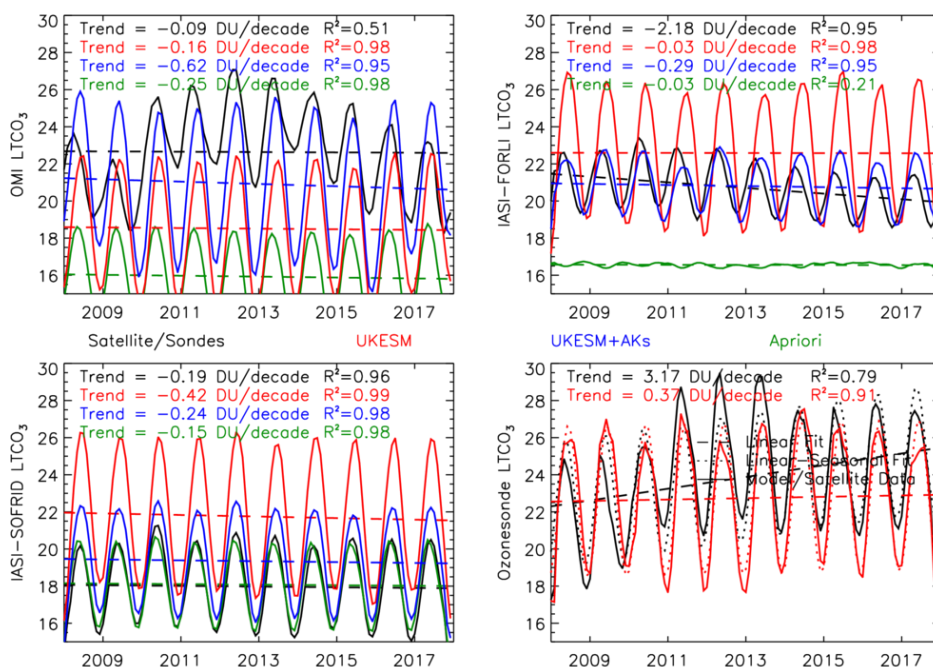
728  
 729 **Figure 1:** Lower tropospheric column ozone ( $LTCO_3$ , surface to 450 hPa, DU) regional time-series for North  
 730 America, based on the HTAP land mask, from OMI (top-left), IASI-FORLI (top-right), IASI-SOFRID (bottom-left)  
 731 and ozonesondes (bottom-right) are shown by the black lines in the respective panels. UKESM simulations  
 732 without and with satellite averaging kernels (AKs) applied are shown in red and blue lines. Green lines show  
 733 the satellite apriori. Dashed lines show the  $LTCO_3$  linear trend which are labelled in the top of each panel. The  
 734  $R^2$  squared values show the linear-seasonal trend model fit to the corresponding  $LTCO_3$  time-series (i.e.  
 735 correlation squared).





736

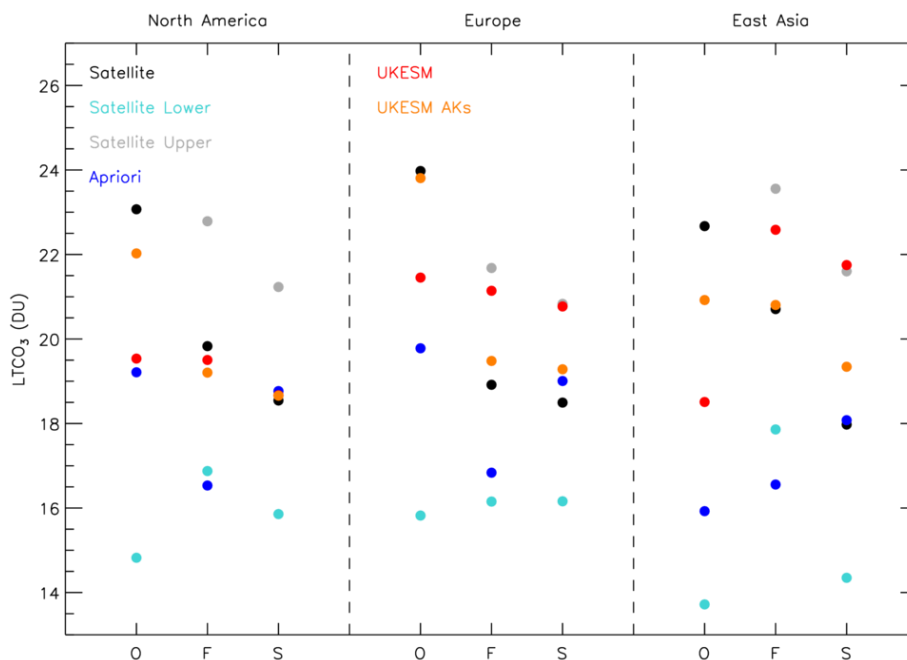
737 **Figure 2:**  $LTCO_3$  (DU) regional time-series for Europe, based on the HTAP land mask, from OMI (top-left), IASI-  
 738 FORLI (top-right), IASI-SOFRID (bottom-left) and ozonesondes (bottom-right) are shown by the black lines in  
 739 the respective panels.. UKESM simulations without and with satellite AKs applied are shown in red and blue  
 740 lines. Green lines show the satellite apriori. Dashed lines show the  $LTCO_3$  linear trend which are labelled in the  
 741 top of each. The  $R^2$  squared values show the linear-seasonal trend model fit to the corresponding  $LTCO_3$  time-  
 742 series (i.e. correlation squared).



743

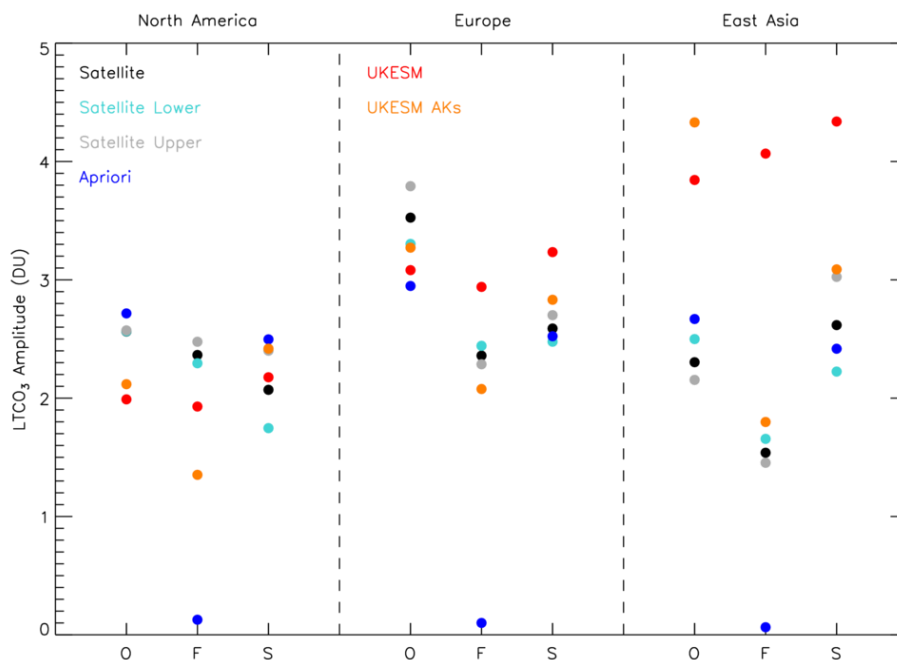
744 **Figure 3:**  $LTCO_3$  (DU) regional time-series for East Asia, based on the HTAP land mask, from OMI (top-left),  
 745 IASI-FORLI (top-right), IASI-SOFRID (bottom-left) and ozonesondes (bottom-right) are shown by the black lines  
 746 in the respective panels.. UKESM simulations without and with satellite AKs applied are shown in red and blue  
 747 lines. Green lines show the satellite apriori. Dashed lines show the  $LTCO_3$  linear trend which are labelled in the  
 748 top of each panel. The  $R^2$  squared values show the linear-seasonal trend model fit to the corresponding  $LTCO_3$   
 749 time-series (i.e. correlation squared).

750



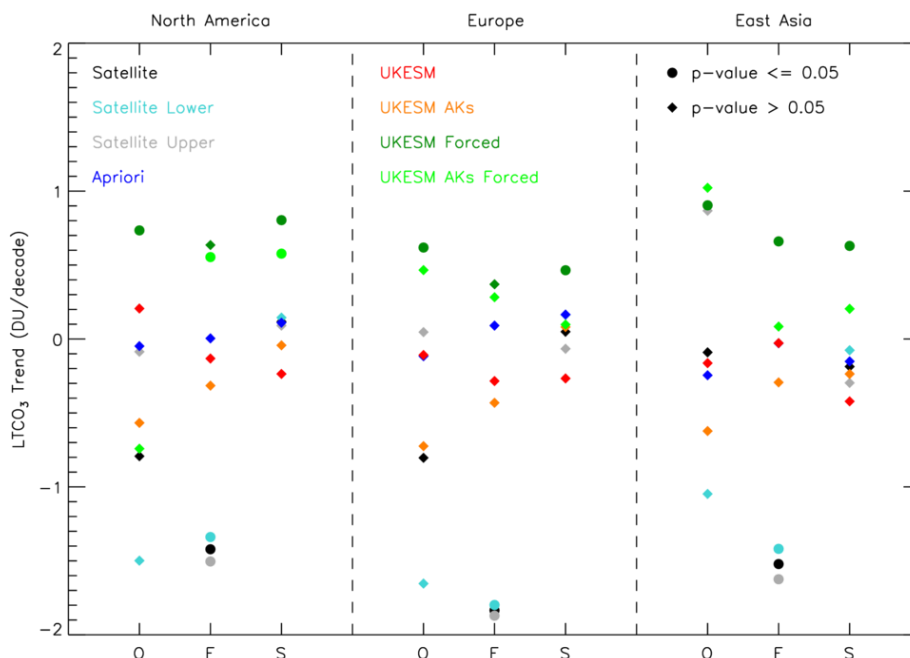
751

752 **Figure 4:** Average  $LTCO_3$  (DU) values across the 2008-2017 time-period for the satellite (black), satellite-lower  
 753 (cyan), satellite-upper (grey), apriori (blue), UKESM (red) and UKESM+AKs (orange). The satellite-lower and  
 754 satellite-upper values are the average of the satellite  $\pm$  its error term time-series (note: these values do not  
 755 always fit in the y-axis range). O, F and S represent OMI, IASI-FORLI and IASI-SOFRID for North America (left),  
 756 Europe (centre) and East Asia (right).



757

758 **Figure 5:** Average  $LTCO_3$  seasonal cycle amplitude (DU) values across the 2008-2017 time-period for the  
 759 satellite (black), satellite-lower (cyan), satellite-upper (grey), apriori (blue), UKESM (red) and UKESM+AKs  
 760 (orange). The satellite-lower and satellite-upper values are the average of the satellite  $\pm$  its error term time-  
 761 series (note: these values do not always fit in the y-axis range). O, F and S represent OMI, IASI-FORLI and IASI-  
 762 SOFRID for North America (left), Europe (centre) and East Asia (right).



763

764 **Figure 6:** Average LTCO<sub>3</sub> linear trends (DU/decade) values across the 2008-2017 time-period for the satellite  
 765 (black), satellite-lower (cyan), satellite-upper (grey), apriori (blue), UKESM (red), UKESM+AKs (orange),  
 766 UKESM forced (dark green) and UKESM+AKs forced (light green). The satellite-lower and satellite-upper  
 767 values are the average of the satellite ± its error term time-series (note: these values do not always fit in the  
 768 y-axis range). O, F and S represent OMI, IASI-FORLI and IASI-SOFRID for North America (left), Europe (centre)  
 769 and East Asia (right). Triangle and circular symbols represent linear trends with p-values > 0.05 or p ≤ 0.05,  
 770 respectively.

771

772

773

774